

Impacts of Storm Surge Barriers on Drag, Mixing, and Exchange Flow in a Partially Mixed Estuary

 David K. Ralston¹ 
¹Woods Hole Oceanographic Institution, Falmouth, MA, USA

Key Points:

- Storm surge barrier infrastructure reduces the tidal amplitude in the Hudson estuary primarily due to form drag
- Salinity mixing increases near the barrier by 15%–30%, but in the estuary overall mixing decreases 5%–10% due to reduced tidal amplitude
- Stratification in the estuary and the salinity intrusion length increase with the barrier, particularly for low river discharge conditions

Supporting Information:

Supporting Information may be found in the online version of this article.

Correspondence to:

 D. K. Ralston,
dralston@whoi.edu
Citation:

 Ralston, D. K. (2022). Impacts of storm surge barriers on drag, mixing, and exchange flow in a partially mixed estuary. *Journal of Geophysical Research: Oceans*, 127, e2021JC018246. <https://doi.org/10.1029/2021JC018246>

 Received 15 NOV 2021
 Accepted 5 APR 2022

Abstract Storm surge barriers are increasingly being considered as risk mitigation measures for coastal population centers. During non-storm periods, permanent barrier infrastructure reduces the flow cross-sectional area and affects tidal exchange. Effects of barrier structures on estuarine tidal and salinity dynamics have not been extensively examined, particularly for partially mixed estuaries. A nested, high-resolution model is used to characterize impacts of a potential storm surge barrier near the mouth of the Hudson River estuary. Maximum tidal velocities through barrier openings are more than double those in the base case. Landward of the barrier, tidal amplitude decreases on average by about 6% due to increased drag. The drag coefficient with the barrier is about 5 times greater than the base case due primarily to form drag from flow separation at barrier structures rather than increased bottom friction. The form drag scales with barrier geometry similar to previous studies of flow around headlands. Tidal water levels are reduced particularly during spring tides, such that marsh inundation frequency is reduced up to 25%. Strong tidal velocities through barrier openings enhance salinity mixing locally, but overall mixing in the estuary decreases due to reduced tidal velocities. Correspondingly, stratification decreases near the barrier and increases landward in the estuary. The salinity intrusion length increases by 5%–15% depending on discharge due to the decreased mixing and increased exchange flow. Exchange flow increases near the barrier due to reflux into the lower layer with the increased mixing, which has the potential to increase estuarine residence times.

Plain Language Summary Storm surge barriers are increasingly being considered as mitigation strategies for flooding of coastal cities. Barrier infrastructure partially blocks tidal flow during non-storm periods and can alter conditions inside the estuary. A high-resolution numerical model is used to assess potential impacts of a storm surge barrier on the Hudson River estuary. In the barrier openings, tidal velocities are more than doubled compared to present conditions. Increased bottom friction and form drag from flow through barrier openings results in a sharp decrease in tidal amplitude inside the estuary. The increase in drag with the barrier is comparable to drag from topographic features like sharp headlands. Mixing of fresh and salt water increases near the barrier due to the greater velocities, but inside the estuary mixing decreases along with the tidal amplitude. As a result, salinity stratification increases in the estuary and salty water moves farther landward. Changes to the circulation patterns with the barrier have potential implications for biogeochemical processes and human uses of the estuary. For example, the barrier would decrease marsh inundation frequency along the estuary and increase the risk of salinity contamination of drinking water supplies drawn from the tidal river.

1. Introduction

Due to sea level rise, increased intensity of coastal storms, and continued growth of coastal populations, flooding due to storm surge increasingly threatens lives and property in coastal cities around the world (Vitousek et al., 2017; Vousdoukas et al., 2018; Wahl et al., 2017). To reduce the risks and impacts associated with storm surge, a potential mitigation measures include ecosystem-based approaches like wetland restoration or artificial reefs, conventional coastal engineering with seawalls or shoreline hardening, and managed retreat from vulnerable areas (Temmerman et al., 2013). For cities with dense populations, valuable infrastructure, and limited space, construction of gated storm surge barriers can be an effective means for establishing or improving coastal flood protection.

Gated storm surge barriers can be closed temporarily during coastal storm events to prevent flooding in the basin landward of the barrier, and during non-storm periods the gates remain open to tidal exchange and navigation. Fewer than 20 storm surge barriers have been constructed globally, but the rate of construction and size of the

barriers have been increasing in the past decade (Mooyart & Jonkman, 2017). Barriers have predominantly been built on broad, shallow deltas (e.g., Eastern Scheldt, New Orleans), in tidal rivers (e.g., Thames River, Ems River), or in small harbors with limited freshwater inputs (e.g., New Bedford, New Haven). Most of the existing barriers are modest in size, as only six are greater than 1 km in length and only three have individual gate openings of 200 m or more (Mooyart & Jonkman, 2017).

Constriction of the tidal flow through open gates increases tidal velocities, which can have negative impacts on navigation and cause scour around barrier support structures. Flow constriction and acceleration through open gates can also affect tidal propagation, affecting the tidal amplitude and circulation patterns in the basin interior. The Eastern Scheldt in the Netherlands, a shallow, well-mixed estuary with modest freshwater inputs, has the most extensive documentation of changes after storm surge barrier construction (Brand et al., 2016; Nienhuis & Smaal, 1994). Barrier construction was completed in 1986 as part of the Delta Works project, and that along with damming of side embayments to reduce the tidal prism caused the mean tide range in the Eastern Scheldt to decrease from 3.70 to 3.25 m (Nienhuis & Smaal, 1994). Decreased tidal currents after barrier construction caused increased stratification, reduced suspended sediment concentrations, increased water column transparency, and a shift in the phytoplankton assemblage (Bakker et al., 1990). Reductions in high tide water level reduced inundation frequency and changed the vegetation species composition in surrounding marshes (de Leeuw et al., 1994). Decreased tidal currents also increased water residence times by a factor of 2–3 (Nienhuis & Smaal, 1994). The barrier and reduced velocities led to a reduction in sediment supply from seaward sources and subsequently to the erosion of tidal flats and loss of critical habitat for wading shorebirds (de Vet et al., 2017).

The Eastern Scheldt is shallow, has large tides, and minimal freshwater inputs, and was a well-mixed estuary prior to barrier construction. Effects of surge barriers on the physical conditions in partially mixed estuaries, which typically are deeper, have more freshwater input, and are more stratified, have not been documented observationally. A modeling study on Chesapeake Bay provides some guidance on the potential impacts of surge barriers on partially mixed estuaries (Du et al., 2017). Barrier configurations blocking 60% and 85% of the flow cross-section were examined and corresponded with reductions in the M2 tidal amplitude of 13%–20%. With the barriers, the salinity intrusion and stratification increased, estuarine exchange flow decreased, and water residence time increased.

In the aftermath of flooding due to Hurricane Sandy, storm surge barriers to protect the New York City region have been examined by the US Army Corps of Engineers (USACE) (Chen et al., 2020; US Army Corps of Engineers, 2019). In 2012, the total water level from Hurricane Sandy was 3.4 m above Mean Sea Level, which was the highest since at least 1700 (Orton et al., 2016; Talke et al., 2014). Flooding from Sandy caused dozens of deaths and damages in excess of \$60B (Strauss et al., 2021). With sea level rise, predictions of annualized coastal flood risk costs for the New York City area are projected to increase from \$5.1B yr⁻¹ to \$13.7B yr⁻¹ by 2100 (US Army Corps of Engineers, 2019). A feasibility study examined several potential storm surge barrier configurations intended to reduce the flooding risk to the New York City region (US Army Corps of Engineers, 2019). The most favorable barrier configuration in the study, described in more detail below, would include a gated opening for the main navigation channel that would be the largest in the world at 430-m wide, superseding the 360-m span of the Maeslant Barrier in the Netherlands (Kluijver et al., 2019). New York is not alone among coastal regions considering major surge barriers. For example, the US Army Corps of Engineers (USACE) is involved in studies for barriers for Galveston Bay to protect Houston, Texas (US Army Corps of Engineers, Galveston District and Texas General Land Office, 2021), for subestuaries of Chesapeake Bay to protect Norfolk, Virginia (US Army Corps of Engineers, Norfolk District and City of Norfolk, 2018), and for parts of the New Jersey Back Bays region (US Army Corps of Engineers, Philadelphia District, 2021).

The surge barrier being considered to protect New York City is located at the mouth of the Hudson River, a partially mixed estuary that differs in physical characteristics from estuaries currently with storm surge barriers. To develop a more quantitative understanding of the potential impacts of a realistic storm surge barrier on a partially mixed estuary, this study examines potential changes in the tidal and estuarine dynamics with the conceptualized barrier design. The approach builds on previous modeling studies of the Hudson by increasing the model grid resolution to better represent the tidal flow through open barrier gates. Barrier and baseline cases are compared for changes in tidal amplitude, salinity intrusion, and stratification across a range of discharge conditions. The momentum budget is evaluated for changes in the total drag coefficient, and differences in the salinity distribution are linked to changes in the mixing and exchange flow. The results are relevant to decisions

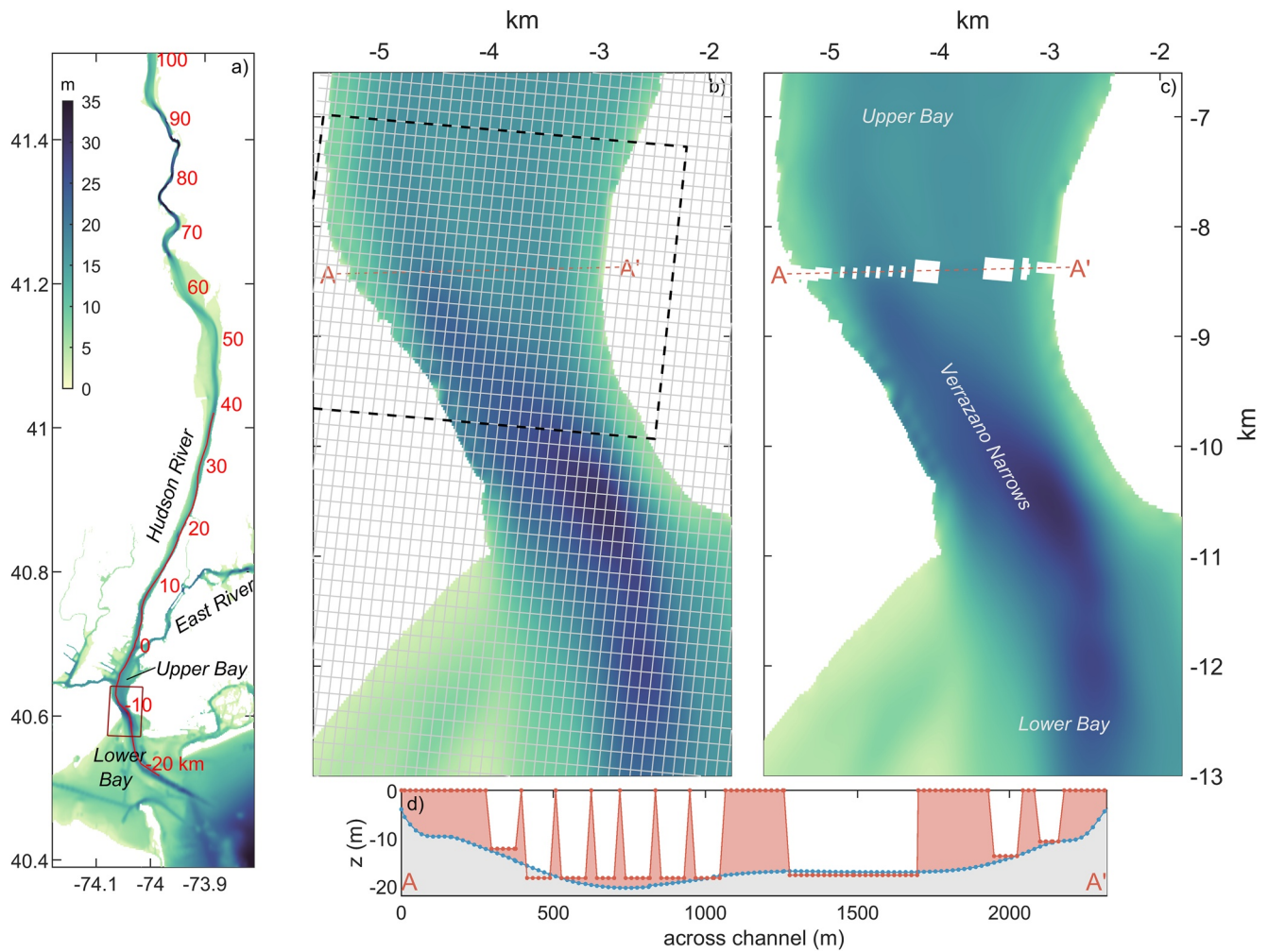


Figure 1. Model bathymetry. (a) Lower Hudson River and New York Harbor in outer grid; the full grid extends north to the tidal limit of the Hudson and includes regions to the east (Western Long Island Sound) and west (Newark Bay, Arthur Kill). Distance from The Battery (km) and the locations of the nest zoom and the along-channel transect in Figure 4 are marked in red. (b) Zoom on center of nest grid at Verrazano Narrows for base case. Gray lines mark every fifth grid cell, and A-A' marks the cross-section in the lower panel. The black box outlines the control volume for the drag calculations. (c) Center of nest grid for barrier cases. (d) Cross-section at location of barriers, with bathymetry for base case (blue markers) and barrier case (red markers).

regarding surge barriers protecting New York City region, but the dynamical changes apply broadly to barriers in other partially mixed estuaries.

2. Methods

The Regional Ocean Modeling System (ROMS) is used to simulate the hydrodynamics and salinity distribution in the Hudson River estuary. Regional Ocean Modeling System (ROMS) is a free-surface, terrain-following, structured grid numerical ocean model (Haidvogel et al., 2008; Shchepetkin & McWilliams, 2005). The model set-up builds on several previous studies of the Hudson using Regional Ocean Modeling System (ROMS) (Ralston et al., 2012, 2013; Warner et al., 2005, 2020). In this application, the model grid is modified to use a nested grid approach to provided higher resolution of the potential storm surge barriers. The outer grid extends the tidal limit at Troy, NY and has open boundaries in New York Bight and Western Long Island Sound (Figure 1). The outer grid is 500 cells by 1,200 cells, with horizontal resolution of 100–200 m in the along-channel direction and 50–100 m across-channel in the estuary. The nested, inner grid is centered on Verrazano Narrows between Upper and Lower New York Bay (Figure 1), increasing the grid resolution by a factor of five in this region. The inner grid is 267 cells by 282 cells, with horizontal resolution of 25–30 m in the along-channel and 20 m in the

across-channel. Nesting is two-way, with information exchange between the outer and inner grid each time step. The model has 16 uniformly spaced layers in the vertical and uses the generic length scale turbulence closure with Kantha-Clayson quasi-equilibrium stability functions. A constant, uniform, low level of horizontal viscosity of $0.5 \text{ m}^2 \text{ s}^{-1}$ is applied to aid in numerical stability. The external time steps are 6.0 s for the outer grid and 1.0 s for the inner grid.

Model simulations were run in two modes: with realistic forcing for a period in 2004 with observations for model calibration and with idealized forcing for analysis of barrier impacts. For forcing at the open boundaries, tidal amplitudes were extracted from the ADCIRC database (Mukai et al., 2002). For the realistic forcing case, nine harmonic constituents were used (K1, O1, Q1, M2, S2, N2, K2, M4, M6). For the idealized forcing cases, tides were simplified to just the three largest components (M2, S2, and N2), but the amplitude of each increased by 30% to maintain a similar total tidal amplitude as the realistic forcing. Idealized tides simplify the analysis by reducing the influence of minor tidal constituents but retaining spring-neap variability with monthly differences between apogean and perigean tides.

River discharge was input at the head of tides. For the realistic forcing, discharge was taken from U. S. Geological Survey observations at Green Island (#1358000) and increased by a factor of 1.4 to account for freshwater inputs from seaward tributaries (Wall et al., 2008). For the idealized forcing, cases with constant river discharges of 125, 500, and 2,000 $\text{m}^3 \text{ s}^{-1}$ were run. These represent low (fifth percentile), average (50th percentile), and high discharge conditions (98th percentile) based on the long-term record at Green Island increased by the factor of 1.4 for seaward tributaries. Wind forcing was specified in the realistic case as spatially uniform and time-varying using data from Newark Airport (NJ). Wind forcing was not included in the idealized cases. For the idealized cases, the analysis period occurred after simulations had adjusted to quasi-steady state, with the salinity distribution varying at the monthly time scale with the tidal forcing but without longer term trends.

Model bathymetry was based on data from New York State Department of Environmental Conservation, the National Oceanic and Atmospheric Administration, and the U.S. Army Corps of Engineers (Ralston & Geyer, 2019). Regions discussed in the analysis include the Lower Hudson estuary extending north of The Battery, Upper Bay located between The Battery and Verrazano Narrows, and Lower Bay located seaward of Verrazano Narrows (Figure 1). Distance along the Hudson is reported relative to The Battery as in previous studies (in river km, or rkm), but the salinity distribution and estuarine dynamics are continuous to the ebb shoals at the entrance to Lower Bay (Ralston & Geyer, 2019).

In addition to the base case, the model grid was adapted to represent a plausible barrier configuration at Verrazano Narrows. Barrier geometry was based on a conceptual design analysis in the New York–New Jersey Harbor and Tributaries Coastal Storm Risk Management Feasibility Study Interim Report (US Army Corps of Engineers, 2019). The report examines several potential configurations for surge barriers around New York Harbor. The focus here is on the conceptual design for a surge barrier just north of Verrazano Narrows, the main entrance to Upper New York Bay. The total cross-sectional flow area at the conceptualized barrier location is 33,000 m^2 . The barrier would have a primary navigational passage 430 m wide and a total width of 980 m for the navigational passage including the piers for the sector gates. A secondary navigational passage located east of the main channel would be 60 m wide, with a total width of 140 m including the piers. Auxiliary flow lift gates span the remainder of the cross-section, each with an open flow width of 46 m and total width of 56 m. Total area open to flow in the conceptualized design is 19,300 m^2 , or 58.5% of the existing flow area. In the model grid, the horizontal grid resolution in the nest of about 20 m cannot represent well the flow through auxiliary flow gates as they are designed (~ 2 grid cells), so the auxiliary flow gates in the model grid are combined to be twice the designed width (92 m opening, total width of 110 m). Sill depths of the gate openings in the model are prescribed as in the conceptualized design: 18 m for the primary navigational passage, 14 m for the secondary navigational passage, and 6–18 m for the auxiliary gates. The total area open to flow in the model grid is 58.3% of the cross-section, similar to the conceptualized design.

For model calibration, results with realistic forcing were compared against observations of water level, velocity, and salinity at locations along the estuary in 2004. Details on the model calibration and skill assessment are provided in the Supporting Information S1. The bottom roughness was adjusted to maximize model skill, resulting in z_0 of 0.5 mm. The skill scores for water level and velocity were nearly the same for cases with $z_0 = 1.5$ and 0.5 mm, but the lower value of z_0 gave slightly higher skill for bottom salinity. Model skills are similar to those

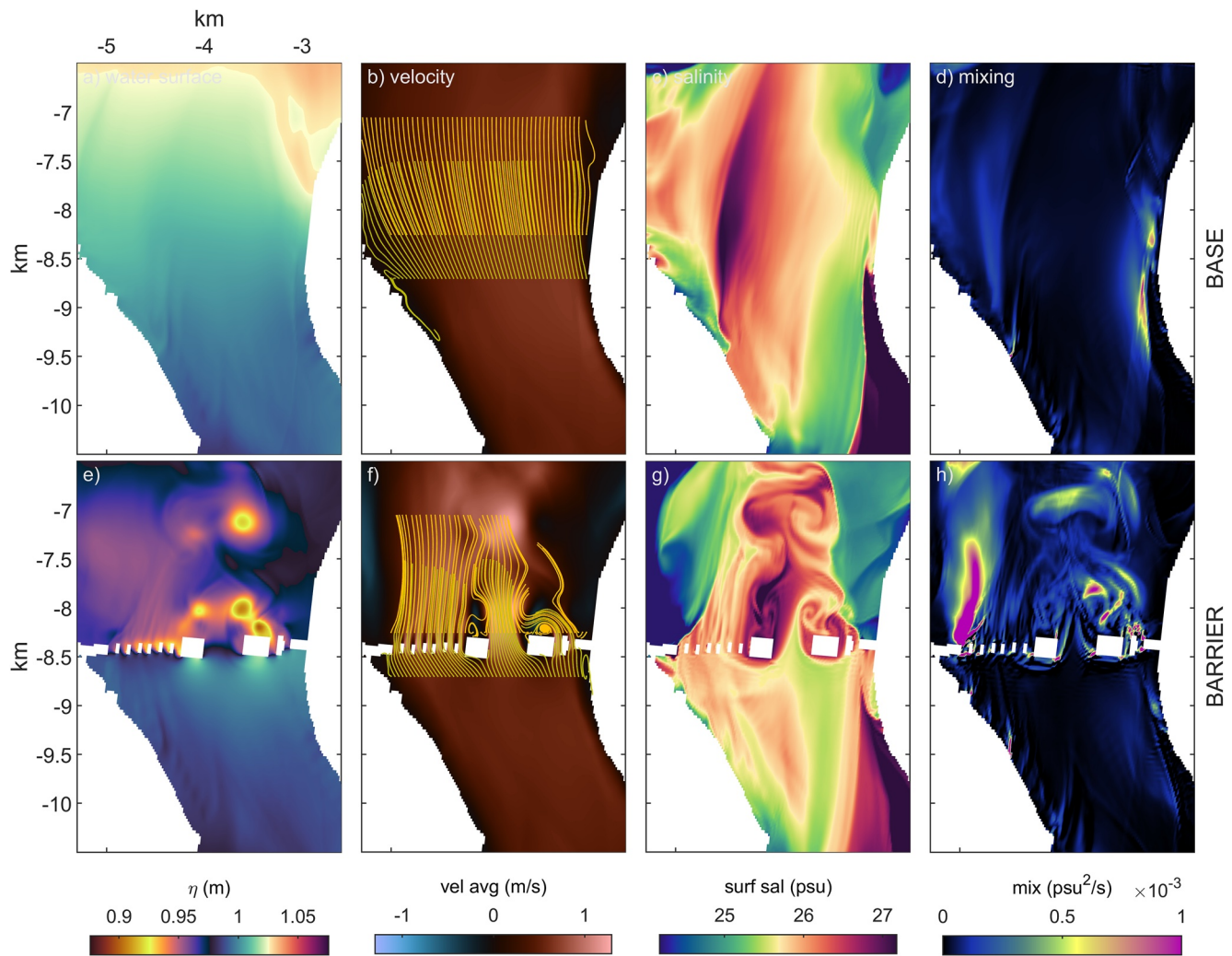


Figure 2. Snapshots of conditions during a spring flood tide (day 22.6, see Figure 5a) for the (a–d) base case and (e–h) barrier case. (a and e) Water surface elevation; (b and f) northward velocity, with streamlines traced from starting locations north and south of the barrier location; (c and g) surface salinity; (d and h) depth integrated salinity mixing.

for the previous grid configuration, which had a similar number of grid cells as the new outer grid but no nesting (Warner et al., 2020). Calibration of the previous grid found an optimal $z_0 = 2$ mm, greater than found here. The new grid configuration has finer grid resolution in the lower estuary, allowing for greater resolution of bathymetric features and flow structure. Lower values of z_0 were also found to be optimal with increasing grid resolution in a model study of the Connecticut River estuary (Ralston et al., 2017). Note that the drag coefficient for bottom friction increases less than linearly with z_0 . For example, assuming a typical depth water depth of 15 m, the three-fold increase in z_0 from 0.5 to 1.5 mm corresponds with an increase in the depth-averaged drag coefficient of about 30% (Lentz et al., 2017).

3. Results

3.1. Flow Near the Barrier

The reduction in flow area through the surge barrier openings causes local alterations to the tidal water surface, velocity field, salinity distribution, and mixing intensity compared to the base case. The bathymetry at the barrier location is the only difference between the baseline and barrier cases, so all the differences in the estuary at larger scales result from changes in flow conditions there. Example conditions are shown for the base and barrier cases during a spring, flood tide with moderate discharge ($500 \text{ m}^3 \text{ s}^{-1}$) (Figure 2). A complementary snapshot during

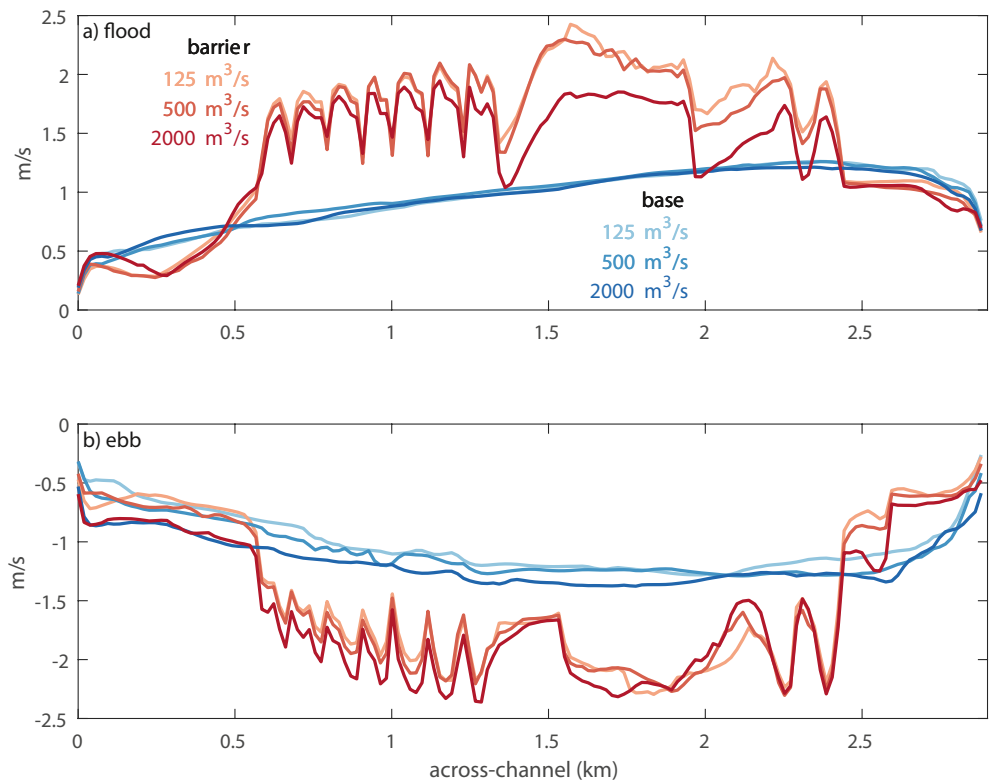


Figure 3. Maximum depth-averaged tidal velocity for (a) flood and (b) ebb. Low, moderate, and high discharge results are shown for the base case (blue lines) and barrier case (red lines).

the subsequent ebb is provided in the Supporting Information S1. In the case with the barriers, velocities through the openings are greater than in the base case. Flow separation occurs downstream of the barriers (landward during flood and seaward during ebb), creating regions of low velocity in the lee of the piers. The flow separation zones have local minima in water surface elevation, and low-pressure eddies are periodically shed and advect with the tidal currents. A sharp drop in water surface elevation occurs across the barriers in the cross-section average. Streamlines calculated from the depth-averaged velocity fields illustrate recirculation zones downstream of the barrier piers corresponding with the eddies in the water surface elevation field.

The surface salinity fields downstream of the barriers reflect the complex structure of the eddy field. During flood tide, the center of the channel has higher salinity compared to the sides downstream (landward) of the barriers due to differential advection of the along-estuary salinity gradient by the higher velocities through the openings and trapping of lower salinity water at the channel edges (Figure 2). During ebb tides the opposite is the case, with fresher water near the main flow openings and saltier water trapped in the lee of the barriers, particularly on the eastern side (Figure S4 in Supporting Information S1). During both phases of the tide the lateral trapping of salinity is enhanced by the barriers, but lateral trapping also occurs in the base case due to flow curvature at the headland on the east side of Verrazano Narrows (Geyer & Signell, 1992). During both flood and ebb, vertical mixing of salinity is enhanced downstream of the barriers compared to the base case (Figures 2 and S4 in Supporting Information S1). Regions of enhanced mixing occur where there are strong spatial gradients in velocity and salinity from the flow through barrier openings.

Constriction of the flow through the barrier openings results in depth-averaged velocities that are greater than the base case by about a factor of 2 (Figure 3). Maximum tidal velocities in the barrier openings are 2 m s^{-1} or greater during both flood and ebb. The increase in tidal velocity extends over a region at least 2 km away from the barriers, where the maximum tidal velocities increase by at least 0.5 m s^{-1} . The maximum tidal velocities depend moderately on river discharge (Figure 3), with the high discharge case ($2,000 \text{ m}^3 \text{ s}^{-1}$) having stronger ebbs and weaker floods than the lower discharge cases, but the variability with discharge is small compared to the effect of the barriers. Surface velocities are greater than the depth-averaged velocities, and the alteration to

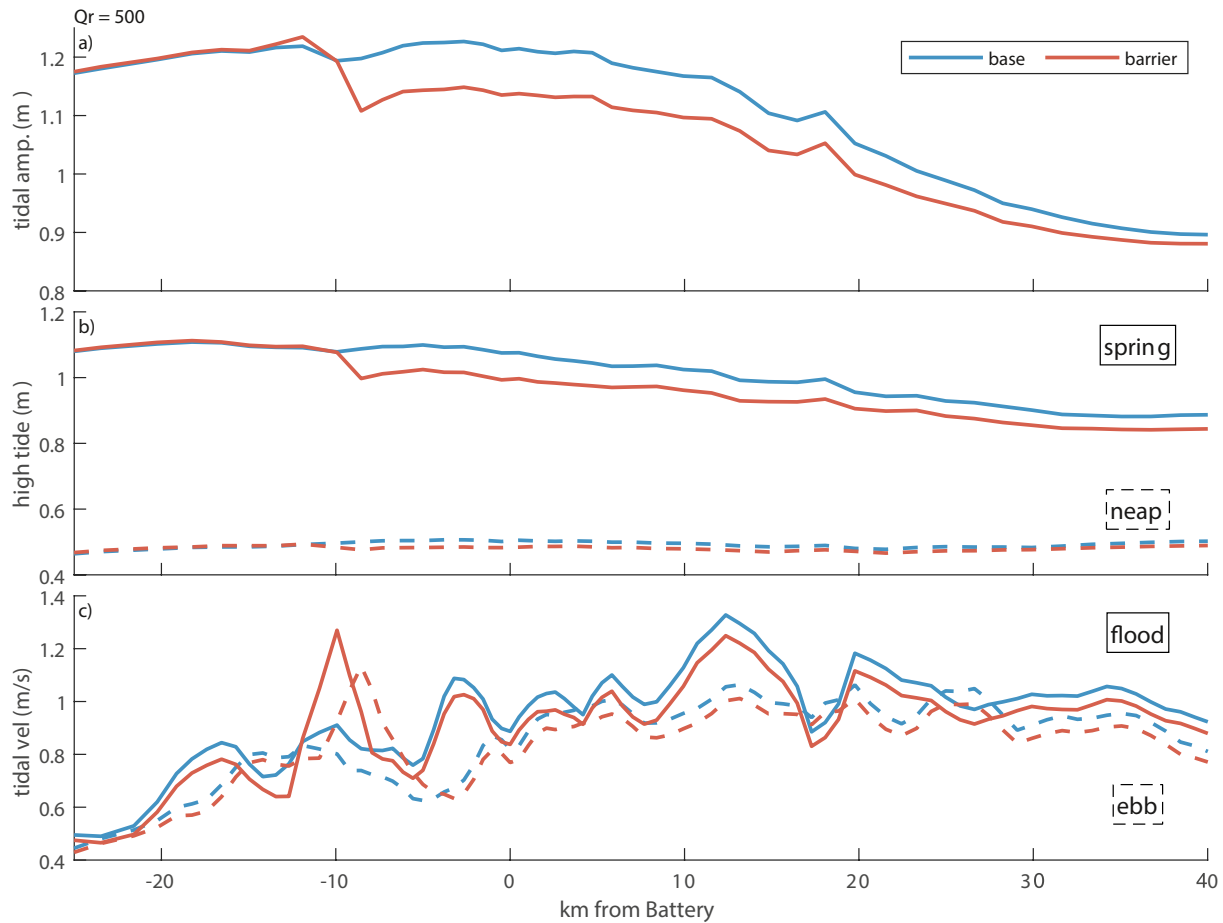


Figure 4. Tidal conditions along the estuary for the base (blue lines) and barrier case (red lines). (a) Tidal amplitude; (b) high tide elevation during spring tides (highest 5% of tidal high waters, solid lines) and neap tides (lowest 5% of high waters, dashed lines); (c) tidal velocity amplitude during flood (solid lines) and ebb (dashed lines).

flow at the surface by the barrier piers has greater tidal asymmetry (not shown). During flood tides in both the base and barrier cases the maximum surface velocities are 10%–20% greater than the depth averages. During ebb tides, flow in the base case is more strongly sheared due to the influence of stratification so that surface velocities are 20%–50% greater than the depth average, and the shear increases with river discharge. With the barrier, ebb surface velocities are only 10%–20% greater than the depth averages because stronger vertical mixing reduces the stratification and shear. However, the increase in velocity due to the flow constriction outweighs the reduction in velocity shear, so surface velocities in the barrier openings ($2\text{--}2.5\text{ m s}^{-1}$) exceed those in the base case ($1.5\text{--}2\text{ m s}^{-1}$).

3.2. Tidal Amplitude and Velocity

The reduction in flow area and increases in tidal velocity at the barrier openings (Figure 3) increase the hydrodynamic drag that removes momentum and energy from the tidal flow. As a result, the tidal amplitude decreases landward of the barrier (Figure 4). Tidal amplitude is calculated from water level time series along the estuary with harmonic fits to tidal constituents, which are predominantly M2, N2, and S2. With the barriers, tidal amplitude in the lower Hudson (<30 rkm) decreases by about 6% (range 3%–8%), and in the upper estuary the average decrease is about 2% (range 1%–3%). The sum of the tidal constituent amplitudes is plotted, but fractional decreases in the M2 component are similar to the total. The effects of the barrier on the tides are greater during spring tides than during neaps, consistent with the increased tidal velocities and increased drag near the barriers. Typical high water levels during spring tides are reduced by about 8 cm in the lower estuary and 3 cm in the upper estuary (Figure 4). During neap tides, reductions in high water are smaller. The results shown here are for

the moderate discharge case ($500 \text{ m}^3 \text{ s}^{-1}$). Decreases in tidal amplitude are similar for the low discharge case and are slightly greater for the high discharge case. For the higher discharge, the decrease in tidal amplitude in the lower estuary averages 7% (range 6%–8%), and the decrease in the upper estuary averages 9% (range 7%–11%).

Cross-sectional average tidal velocities at the barrier increase by 40%–50% compared to the base case, from 0.8 to 0.9 m s^{-1} to 1.2–1.3 m s^{-1} (Figure 4). This increase in average velocity is consistent with the reduction in cross-sectional area of about 40%. Farther landward in the estuary, the cross-sectional average velocities decrease with the barrier by 5%–10%, similar to the decrease in tidal water level amplitude.

3.3. Drag Increases Near the Barriers

To diagnose the influence of the barrier on the tidal dynamics, we consider the depth-averaged momentum equation:

$$\frac{\partial U}{\partial t} + U \frac{\partial U}{\partial x} = -g \frac{\partial \eta}{\partial x} - \frac{1}{2} \beta g \frac{\partial S}{\partial x} H - \frac{1}{H} \left(-\frac{\partial}{\partial x} \left(v_h H \frac{\partial U}{\partial x} \right) - \frac{\partial}{\partial y} \left(v_h H \frac{\partial U}{\partial y} \right) \right) - C_d \frac{U|U|}{H} \quad (1)$$

where U is along-channel velocity, η is water surface elevation, H is water depth, S is salinity, g is gravitational acceleration, and β is the haline contraction coefficient. The left side consists of the unsteadiness and advective acceleration terms. The right side includes the barotropic and baroclinic pressure gradients, the horizontal viscosity, and the depth-averaged drag force represented with a quadratic drag coefficient C_d . A control volume to calculate the terms of the budget is defined in the nested grid centered on the barrier location and extending about 1 km north and south (Figure 1). Velocity and depth are averaged in the control volume, and gradients of velocity, water level, and salinity are calculated across the control volume.

To quantify the changes in drag resulting from the barriers, an effective drag coefficient is calculated from the momentum budget:

$$C_d = \left(\frac{\partial U}{\partial t} + U \frac{\partial U}{\partial x} + g \frac{\partial \eta}{\partial x} + \frac{1}{2} \beta g \frac{\partial S}{\partial x} H + visc \right) / \left(-\frac{U|U|}{H} \right) \quad (2)$$

where C_d represents the total drag needed to balance the other terms. Here the horizontal viscosity is abbreviated for clarity. The major source of drag in most estuarine flows is the bottom friction, which is determined in the model based on the bottom roughness (z_0) and near-bottom vertical shear. The bottom stress within the control volume is calculated directly from the model results, and that can also be expressed in terms of a quadratic drag coefficient, C_f :

$$C_f = \left(\frac{1}{\rho} \langle \frac{\tau_b}{h} \rangle \right) / \left(-\frac{U|U|}{H} \right) \quad (3)$$

where $\langle \tau_b \rangle$ is the bottom stress, h is the local depth, and $\langle \tau_b/h \rangle$ represents the spatially averaged bottom stress divergence.

The depth-averaged momentum budget terms are shown for the base and barrier cases over two spring-neap cycles (Figure 5). In the base case, the dominant terms are the surface pressure gradient, unsteadiness, and bottom stress. The horizontal viscosity term is an order of magnitude smaller than the advective acceleration, which is the next smallest term. The bottom stress has similar magnitude and phase as the sum of the terms in the numerator of Equation 2 (unsteadiness, advection, the surface and baroclinic pressure gradients, and viscosity), which is consistent with bottom stress being the dominant source of drag in the base case. The average total drag coefficient in the base case is $C_d = 0.0034$. The average drag coefficient calculated from the bottom stress is $C_f = 0.0017$.

The difference between the total and bottom drag coefficients indicates that factors in addition to bottom friction are contributing total drag. The discrepancy between the total drag and bottom friction is tidally asymmetric with a greater difference during ebb tide, as seen in the plots of the momentum budget terms versus $-U|U|/H$ (Figure 5). The C_f for bottom friction is similar in both phases, but the total C_d is greater during ebb than flood. Form drag due to with flow separation around natural features like headlands or sills can be a momentum sink, and this region has complex topography and steeply sloping sidewalls. The snapshot from the base case during

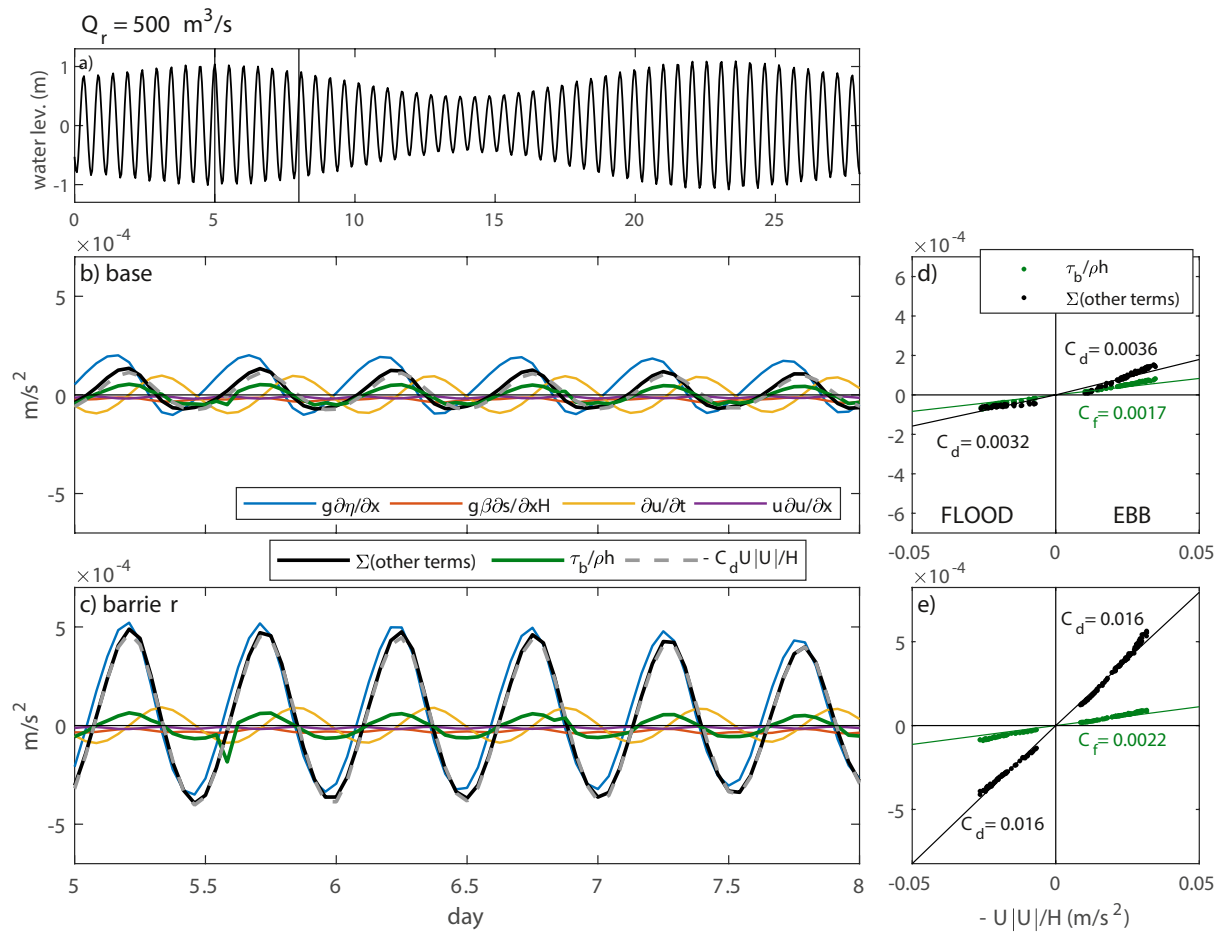


Figure 5. Depth averaged momentum budget near the barrier location for moderate discharge. (a) Tidal water level, with vertical lines marking period shown in lower panels (b and c) Momentum budget terms for the base and barrier cases. (d and e) Bottom friction term (green markers) and sum of momentum budget terms (black markers) versus $U|U|/H$ at each maximum flood and ebb tidal velocity over the period in (a), marking best-fit slopes that correspond with drag coefficients C_f and C_d .

a flood tide (Figure 2) illustrates a region on the west side near headland with flow separation and reversal in streamlines. Such small-scale anomalies occur during both flood and ebb and contribute to the factor of 2 difference between C_f and C_d in the base case.

In the momentum budget with the barrier, the most prominent difference compared to the base case is the increase in the magnitude of the surface pressure gradient term (Figure 5). The next biggest terms are the unsteadiness and bottom friction, as before, but they are much smaller than the pressure gradient. The horizontal viscosity has similar magnitude as the advective acceleration and is an order of magnitude less than the bottom stress. The bottom stress is greater than in the base case such that the average C_f increases to 0.0022, or by about 30%. However, the average total C_d required to balance the other terms increases to 0.016, or by a factor of 5 compared to the total C_d for the base case. The total C_d has similar magnitude between flood and ebb, which is consistent with the similarities in the flow separation and eddy fields generated by the barrier piers (Figures 2 and S3 in Supporting Information S1). The total C_d is calculated based on the average velocity in the control volume, which with the barrier is about 95% of that without the barrier. This small reduction in average velocity is due to the integrated effects of stagnant regions near the piers and accelerations through the barrier openings (Figure 3). With the quadratic drag, the effect of the velocity difference between the cases is about a 10%, which is much smaller than the difference in C_d .

The momentum budget terms are shown only for the moderate discharge case (Figure 5), but the increases in total C_d are similar for the low and high discharge cases (Figure 6). The average total C_d increases by about a factor of

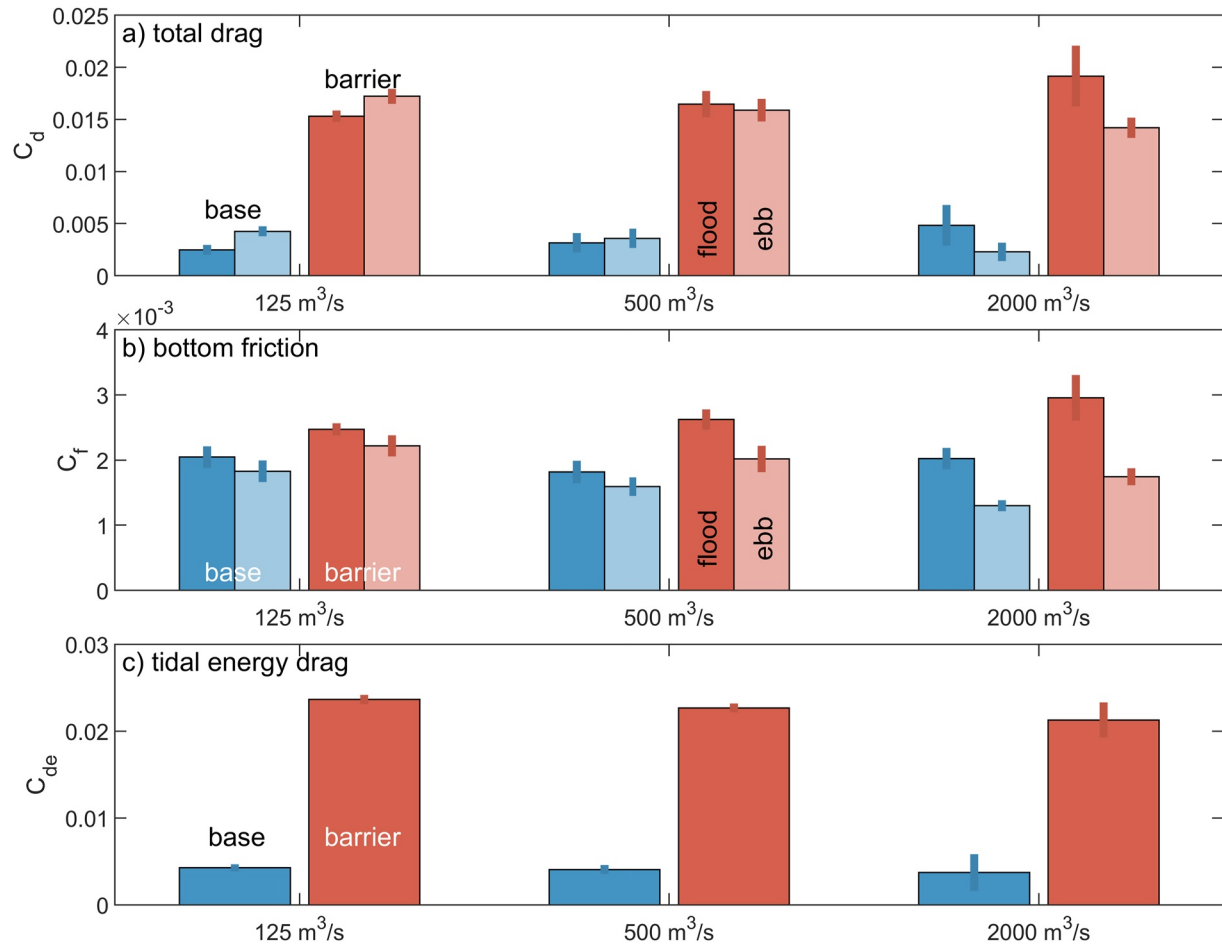


Figure 6. Drag coefficients in the Verrazano Narrows nest region for the base (blue bars) and barrier (red bars) cases under low, medium, and high discharge forcing. (a) Total drag coefficient C_d based on the depth-averaged momentum balance, distinguishing mean values for ebb and flood; (b) bottom friction drag coefficient C_f , distinguishing mean values for ebb and flood; (c) drag coefficient C_{de} based on the tidal energy dissipation.

5 in all three discharge cases. For the high discharge case, C_d is greater during flood tides both with and without the barriers.

The bottom friction C_f increases with the barriers in all three discharge cases, but the increases are 20%–40% and much less than the increases in total C_d (Figure 6). Intensification of the tidal velocities through the barrier openings increases the average bottom friction in the control volume. Weaker stratification with the barrier (discussed below) also contributes to the increase in bottom friction. The C_f values are greater during flood than ebb for both the base and barrier cases, which is consistent with stronger stratification during ebbs. The C_f becomes more tidal asymmetric for the high discharge case because stronger stratification reduces the bottom friction preferentially during ebb tides.

The increase in total drag with the barrier results in a decrease in tidal water level and velocity in the estuary (Figure 4). The decrease in tidal energy flux through the barrier openings provides an alternative means for quantifying the effect on the total drag. The along-estuary change in tidal amplitude can be written as

$$\frac{\partial \|\eta\|}{\partial x} = 0.5(\gamma_w + \gamma_h) \|\eta\| - \frac{4C_{de} \|U\|^2}{3\pi g \bar{H} \cos(\Delta\phi)} \quad (4)$$

where $\|\eta\|$ is the tidal amplitude and $\|U\|$ is the tidal velocity amplitude (van Rijn & Leo, 2011). Width and depth convergence coefficients $\gamma_w = 1/L_w$ and $\gamma_h = 1/L_h$ are based on e -folding scales L_w and L_h for along-estuary gradients in channel width and depth. \bar{H} is the average depth, $\Delta\phi$ is the phase difference between tidal water level and velocity, and C_{de} is a drag coefficient based on the tidal energy flux. The first term on the right side represents

amplification of the tide with channel convergence or shoaling, or the decrease in tidal amplitude with channel widening or deepening. The second term represents the loss in tidal energy due to drag. The drag coefficient can then be written as

$$C_{de} = \left(-\frac{\partial \|\eta\|}{\partial x} + 0.5\gamma_g \|\eta\| \right) \frac{3\pi g \bar{H} \cos(\Delta\phi)}{4\|U^2\|} \quad (5)$$

where the along-channel geometry factors have been combined in a convergence parameter of $\gamma_g = 1/L_g = (\gamma_w + \gamma_h)$. The channel width and depth in New York Harbor and the lower Hudson covary with the local geological constraints, so the geometric length-scale of $L_g = 60$ km is based on the large-scale gradient in cross-sectional area. Convergence length scales of 10–50 km have been reported for other estuaries (van Rijn & Leo, 2011), and being at the high end of this range reflects the relatively uniform width and depth along the lower Hudson. L_g is assumed to be the same for cases with and without barriers because it represents the larger scale convergence that affects shoaling of the tidal wave rather than local perturbations like the barriers. The value of the convergence parameter has ambiguity because the natural bathymetry does not conform to an exponential function, but it does not contribute to differences in C_{de} between the cases because it is assumed to be the same. C_{de} is calculated based on the change in tidal amplitude over the momentum budget control volume.

The drag coefficients based on the tidal energy flux have similar magnitude and variability with the forcing conditions as the total C_d from the momentum budget (Figure 6). Tidal amplitude and phase (M2) are calculated in 5-day blocks and used in Equation 5 to get a time series of C_{de} , but only average values for each case are shown because the temporal variability was small compared to the differences between cases. Without the barriers, C_{de} is around 0.004, consistent with dissipation of tidal energy that is primarily due to bottom friction. With the barriers, C_{de} increases by a factor of about 6, with an average $C_{de} = 0.023$. This estimate of C_{de} has uncertainty associated with the geometric convergence parameter. For example, for $L_g = 40$ km, the average values of C_{de} without and with barriers are 0.006 and 0.025, whereas for $L_g = 80$ km the average C_{de} are 0.003 and 0.021. Therefore, over a reasonable range of convergence length scales the tidal energy flux provides a consistency check on the increase in total drag with the barrier.

3.4. Salinity and Stratification

Increased tidal velocities through the barrier openings, locally increased drag, and reduced tidal amplitude landward of the barrier alter the salinity distribution compared to the base case. In the Hudson, the length of the salinity intrusion depends on both river discharge and tidal amplitude. The salinity shifts seaward during periods of high discharge due to the increased mean outflow, and it shifts seaward during spring tides due to the increased tidal mixing and decreased estuarine exchange flow (Ralston et al., 2008). Alternatively, the salinity intrusion moves landward during low river discharge and neap tides. Seasonally the salinity intrusion can vary between about 30 rkm during the spring freshet and about 120 rkm during summer low discharge, neap tides (Abood, 1974; Bowen & Geyer, 2003).

With surge barriers, the salinity intrusion shifts landward compared to the base case (Figure 7). Here the intrusion is characterized based on the 0.5 psu isohaline of the tidally averaged near-bottom salinity, but results are similar for the 2 psu isohaline. With and without the barriers, the salinity intrusion at low discharge is relatively steady over the spring-neap cycle due to the slow response time with a long estuary (Lerczak et al., 2009). Including the barriers results in a landward shift of the salinity intrusion by 4–6 km, or an increase of 4%–5% compared to the base case. The salinity intrusion with moderate and high discharge displays greater spring-neap variability and the maximum is during the neap-to-spring transition (Ralston et al., 2008). The landward shifts for the moderate discharge case are greater than for the low discharge case and represent a fractional increase of 5%–15% compared with the base case. For the high discharge case the changes were small in both absolute and relative terms.

Stratification in the estuary depends on the length of the salinity intrusion and the strength of the tidal mixing. In the immediate vicinity of the barriers, the increased tidal velocities through the barrier openings increase mixing and reduce stratification. This occurs for all the discharge cases, with an overall reduction in the stratification seaward of The Battery regardless of spring-neap phasing (Figure 8). Farther into the estuary, the increased salinity intrusion and reduced tidal velocities combine to increase stratification. This is most apparent at low discharge where enhanced stratification propagates up the estuary during neap tides with the salinity intrusion (Figure 7).

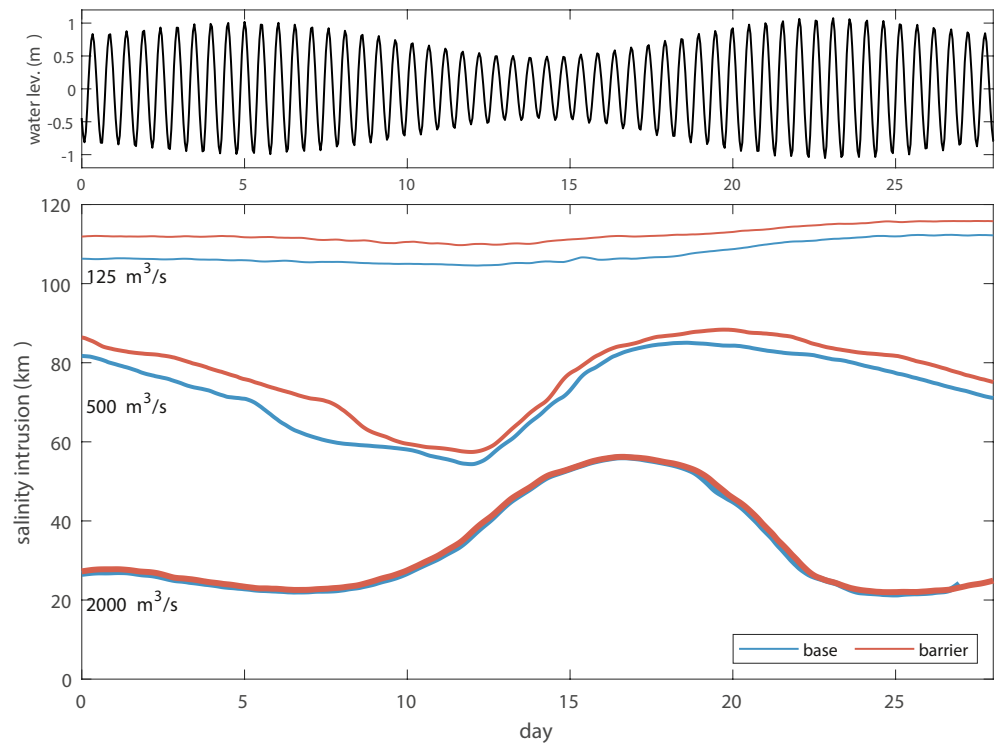


Figure 7. Salinity intrusion for the base (blue lines) and barrier case (red lines). (a) Tidal water level; (b) salinity intrusion location based on the 0.5 psu isohaline for the low, medium, and high discharge forcing.

Stratification shown is the difference between surface and bottom salinity in the thalweg. In all cases, the salinity distribution is more landward and more stratified with the barrier, and this shifts destratification to later in neap tides. This spring-neap lag in the destratification is about 2 days greater with the barrier than in the base case.

3.5. Mixing Increases Near the Barriers and Decreases in the Estuary

The flow constriction causes changes in mixing both locally near the barrier and more broadly within the estuary. To quantify the changes in mixing, we calculate the dissipation of salinity variance (Burchard & Rennau, 2008). The tracer variance calculation includes the explicit, turbulent mixing due to the eddy diffusivity from the turbulence closure as well as the numerical mixing that results from discretization errors in the advection scheme. Including the numerical mixing component is particularly important in regions with sharp spatial gradients in bathymetry, velocity, and salinity, as has been found in the Hudson as well as other estuaries (Ralston et al., 2017; Rennau & Burchard, 2009; Warner et al., 2020).

Comparison of the time-averaged, depth-averaged salinity variance decay for moderate discharge illustrates the local influence of the barrier (Figure 9). Mixing is enhanced near the barrier openings during both flood and ebb tides. The increased mixing extends more than 1 km away from the barriers in the flow direction. Natural variability in the bathymetry and shoreline also affect the spatial distribution of mixing, with enhanced mixing on the lateral shoals and downstream of the headlands that bracket Verrazano Narrows, particularly during ebb tides.

The mixing calculation incorporates both the resolved mixing due to the turbulence closure and the numerical mixing from the advection scheme, and the relative contribution of the numerical mixing increases in the barrier case. In the region within 2 km of the barrier, numerical mixing on average represents 5.9% of the total during flood tides in the base case and 8.2% of the total mixing during ebb tides. In the barrier case, numerical mixing accounts for 15.4% of the total mixing near the barrier during floods and 18.6% of the total during ebbs. This increase in the numerical mixing results from the stronger velocities and generation of sharp salinity gradients at the barrier openings (Figure 2). While increased relative to the base case, the numerical mixing with the barrier is not dominant compared to the turbulent mixing.

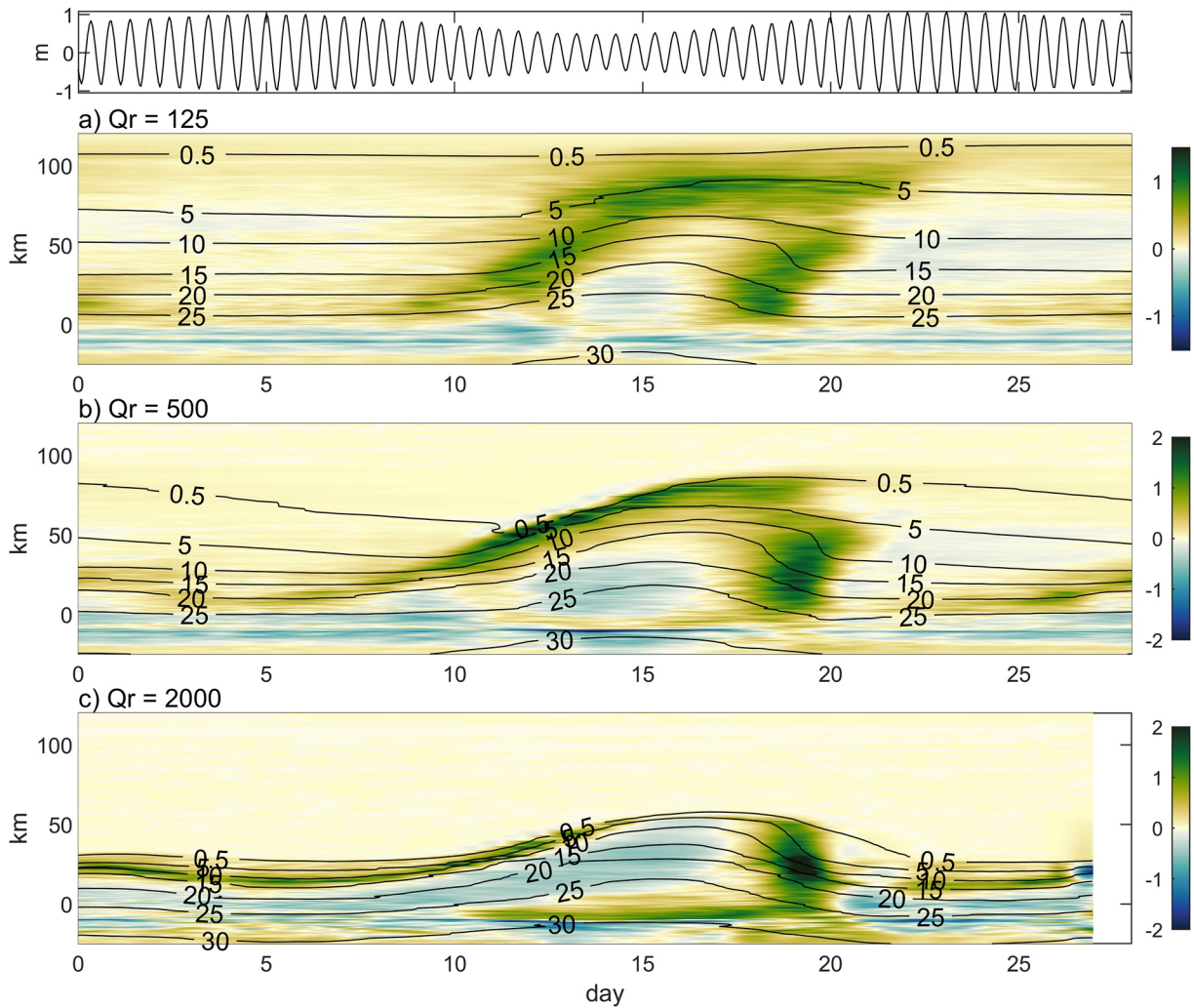


Figure 8. Differences in stratification between the barrier and base cases for (a) low discharge, (b) moderate discharge, and (c) high discharge forcing. Results are tidally filtered, and positive values represent stronger stratification in the barrier case. Labeled contours are near-bottom salinity isohalines, and the top panel shows tidal water level.

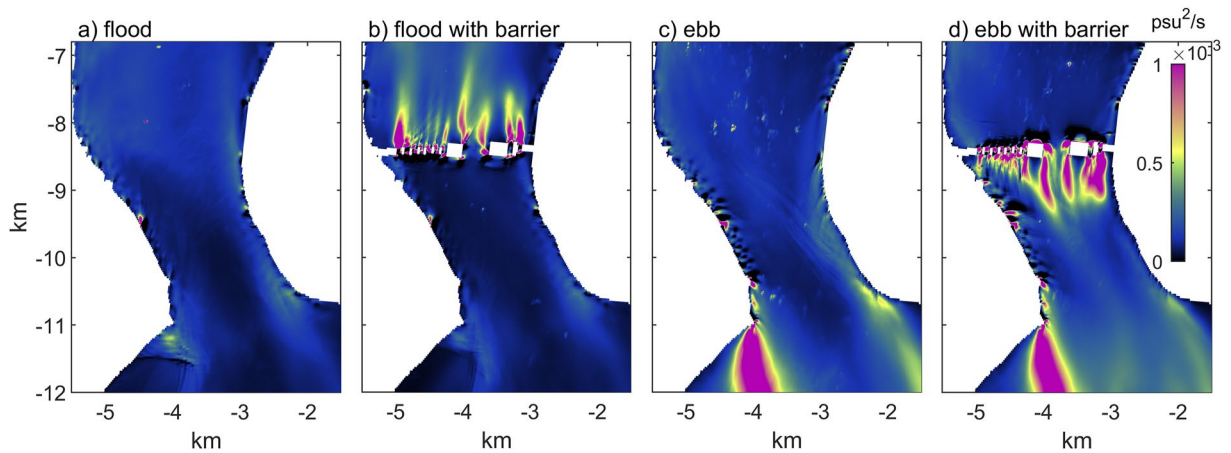


Figure 9. Depth-averaged mixing (combining turbulent closure and numerical diffusion) during (a and b) flood tides and during (c and d) ebb tides for the (a and c) base and (b and d) barrier cases.

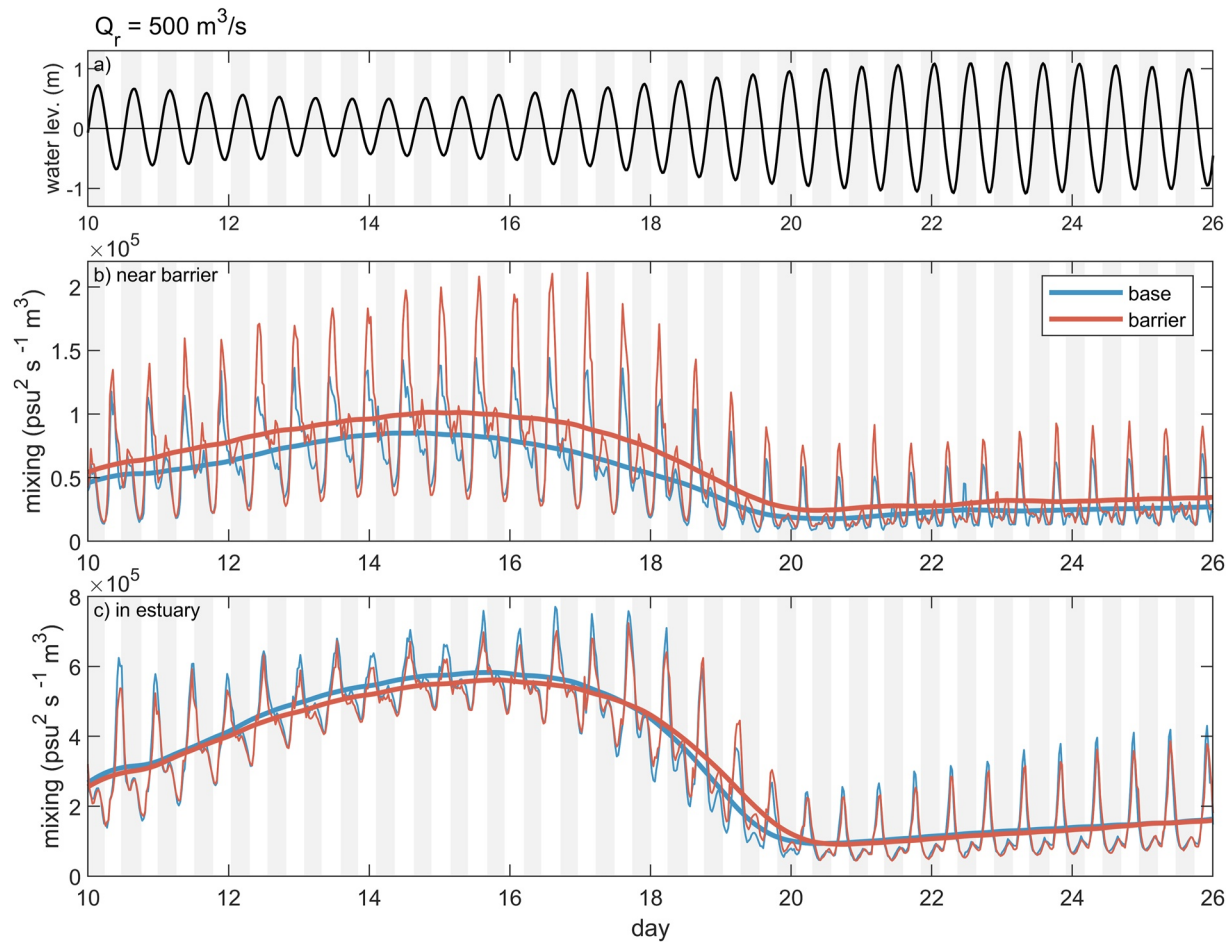


Figure 10. Volume integrated mixing in the base (blue lines) and barrier (red lines) cases for moderate discharge forcing. (a) Tidal water level; (b) volume integrated mixing near the location of the barrier, including tidally varying (thin lines) and tidally averaged (thick lines) quantities; (c) volume integrated mixing in the estuary landward of the barrier, also with tidally varying and tidally averaged values. Gray shading marks flood tides.

The total mixing in the nested grid increases with the barrier during both spring and neap tides, but the difference is greatest during the neap-to-spring transition when stratification is decreasing (Figure 10). Mixing occurs predominantly during ebbs in both cases. The ebb tide peaks in mixing are enhanced with the barrier for the moderate discharge case by up to 50%. On average, mixing in the nested grid during neap tides is increased by about 20% and the increase is about 30% during spring tides. For the low discharge case the average mixing increases by 15%–25%, and for the high discharge case the increase is about 20%.

In the estuary overall, mixing also occurs primarily during ebbs (Figure 10). Previous analysis of salinity variance in the Hudson also found that mixing occurred primarily during ebbs, and was localized to frontal regions near topographic constrictions (Warner et al., 2020). With barrier, the ebb tide peaks in total mixing in the estuary decrease by about 10% compared to the base case. The tidally averaged differences are less than 5% and depend in part on the differences in the stratification and salinity intrusion between the cases. For example, during the neap-to-spring transition (day 18–20) mixing with barrier is greater than in the base case because the estuary remains stratified and can be mixed, whereas in the base case stratification is weak and there is less potential for mixing (Figure 8).

3.6. Exchange Flow Increases Near the Barriers and in the Estuary

The increase in the salinity intrusion with barriers indicates an increase in the landward salt flux. To quantify the salt flux at locations along the estuary we use the total exchange flow (TEF) framework (MacCready, 2011). Total exchange flow (TEF) uses isohaline coordinates to calculate salt transport through a cross-section. Total

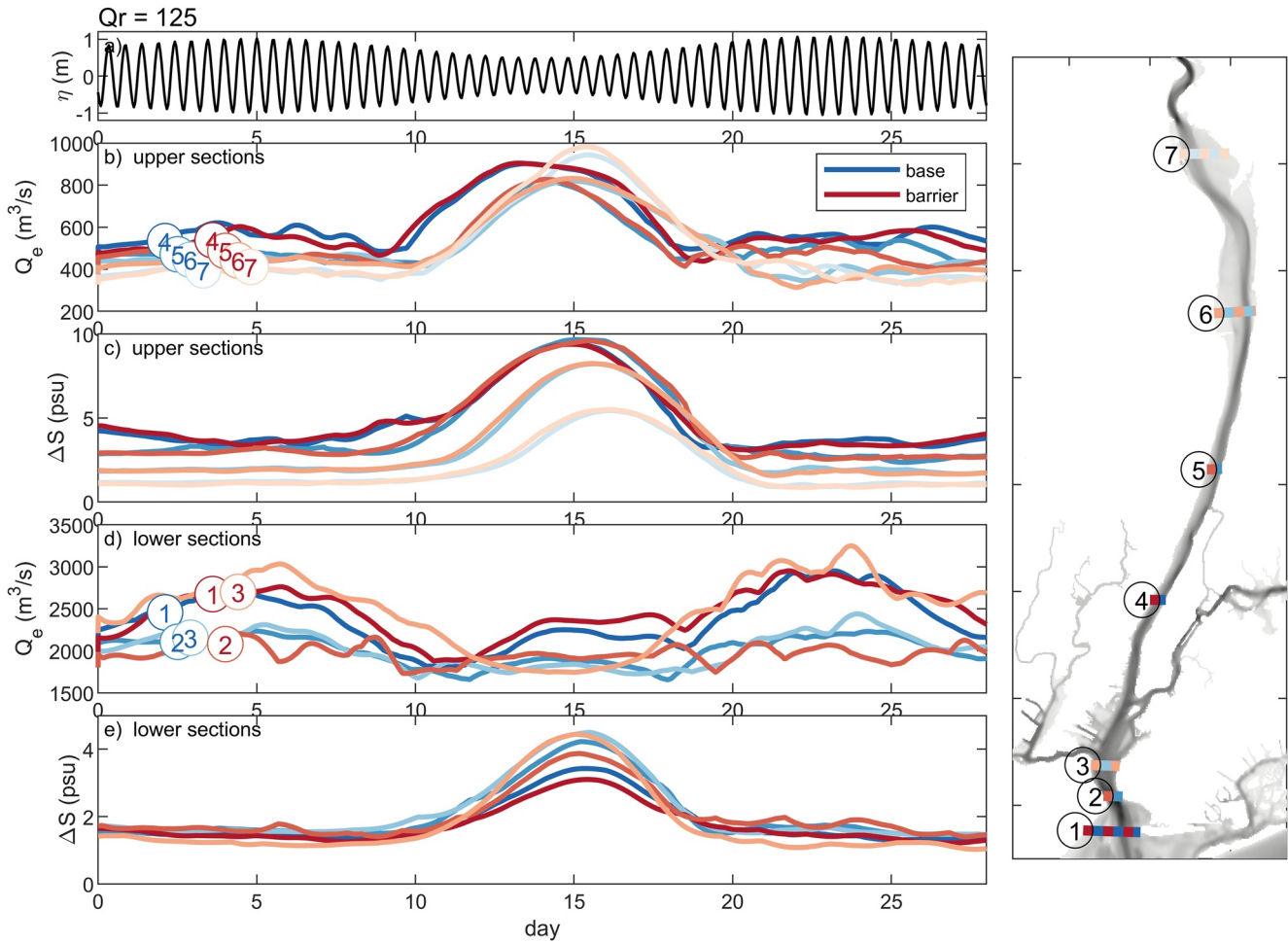


Figure 11. Total exchange flow (TEF) in the base (blue lines) and barrier (red lines) cases at sections along the estuary for moderate discharge forcing. (a) Tidal water level; (b) exchange flow ($Q_e = (Q_{in} - Q_{out})/2$) at four sections along the lower Hudson estuary (locations in map on the right); (c) salinity difference between TEF inflow and outflow $\Delta S = (S_{in} - S_{out})$ at the same sections along the lower Hudson; (d) Q_e at three sections in New York Harbor; (e) ΔS at the same sections in New York Harbor.

exchange flow (TEF) incorporates both the tidal and subtidal components of the salt flux, and has been used to quantify the exchange flow in estuaries with a range of dominant transport processes (Burchard et al., 2018; Chen et al., 2012; Conroy et al., 2020; Rayson et al., 2017; Sutherland et al., 2011).

The exchange flow is calculated at multiple cross-sections through New York Harbor and the lower Hudson (Figure 11). Cross-sections are aligned with the model grid to reduce interpolation errors. At each cross-section, volume and salt transport from hourly output are sorted into salinity classes (0.05 psu interval) and tidally averaged. Inflowing and outflowing components of the transport are distinguished based on the global maximum of $Q(s)$, where Q is the volume transport in salinity bin s (Lorenz et al., 2019; MacCready et al., 2018). The sum of the inflowing volume transport is Q_{in} , and the flux-weighted salinity of the inflow is S_{in} . The outflowing transport and salinity, Q_{out} and S_{out} , are calculated similarly, and Q_{out} is negative in the sign convention.

The tidally averaged, volume integrated salt balance landward of a section can be written as

$$\frac{d}{dt} \int S dV = Q_{in} S_{in} + Q_{out} S_{out} \quad (6)$$

where the left side represents the time rate of change of salinity in the estuary, or correspondingly the length of the salinity intrusion. The exchange flow can be defined as the average of the inflowing and outflowing transport at each cross-section:

$$Q_e = \frac{(Q_{in} - Q_{out})}{2} \quad (7)$$

(MacCready et al., 2021). The mean salinity is the average of the inflowing and outflowing salinities, $\bar{S} = (S_{in} + S_{out})/2$, and the difference between the inflowing and outflowing salinity is analogous to a mean stratification, $\Delta S = S_{in} - S_{out}$. The salt budget can then be rewritten as

$$\frac{d}{dt} \int S dV = Q_r \bar{S} + Q_e \Delta S \quad (8)$$

where the terms on the right represent the balance between the seaward transport by the river flow and the landward transport by the exchange flow (MacCready et al., 2021).

As an alternative to TEF, the volume and salt fluxes at a cross-section can be decomposed spatially and separated into subtidal and tidal components (Fischer, 1972; Lerczak et al., 2006). In much of the lower Hudson, the steady component of the Eulerian exchange dominates the total salt transport, and it is well represented by the exchange flow driven by the salinity gradient (Bowen & Geyer, 2003; Lerczak et al., 2006; Ralston et al., 2008). However, in regions with bathymetric complexity such as constrictions and channel junctions the tidal component of salt flux can be locally enhanced and even greater than the steady component (Geyer & Nepf, 1996). The flow constriction and strong tidal velocities associated with the barriers are likely to enhance the tidal salt flux and to reduce the subtidal salt flux, but TEF approach captures the net effect on the total salt flux.

In the lower Hudson, the exchange flow increases during neap tides and decreases during spring tides due to the inverse dependence of the gravitational circulation on tidal mixing (Figure 11), as has been observed (Lerczak et al., 2006). The low discharge case is shown to illustrate conditions when the salinity intrusion is greatest. Exchange flow generally decreases in the landward direction, consistent with the decreasing salt transport. The effect of the barriers is to moderately increase the exchange flow compared to the base case, particularly during neap tides. Similarly, the TEF stratification ΔS increases during neap tides and is slightly greater with the barriers than in the base case. Thus the reduction in tidal amplitude due to the drag at the barriers leads to increased exchange flow and increased stratification farther up the estuary, and consequently greater salinity intrusion.

In contrast to the lower Hudson, ΔS decreases in New York Harbor with the barrier (Figure 11). The change in TEF ΔS corresponds with the decrease in mean stratification because of the stronger tidal velocities and mixing (Figure 9). However, the effect of the barrier on the exchange flow is more complex. Overall, the exchange flow tends to decrease from the mouth toward the limit of the salinity intrusion, and this is generally true for the base case. With the barrier, this also holds for neap tides, but during spring tides the exchange flow in the Upper Bay is greater than in the more seaward sections (Figure 11).

Strong tidal mixing induced by flow constriction at the barrier contributes to this enhanced exchange flow in the Harbor. The effect of vertical mixing on the exchange flow has been noted in strongly tidal sill regions of Puget Sound and described as complementary processes of efflux and reflux (Ebbesmeyer & Barnes, 1980; MacCready et al., 2021). Efflux is the mixing of deeper, landward flowing water into the surface layer and reflux is the mixing of surface water down into the lower layer. The effect of the reflux is to transfer seaward flowing water upstream of the sill or barrier into the landward flowing lower layer and increase recirculation. With TEF this manifests as a local increase in the exchange flow (MacCready et al., 2021). The Hudson does not have sharp sills separating deep basins as in Puget Sound, but the increase in mixing with the barriers (Figure 9) causes similar reflux and creates a local increase in the exchange flow (Figure 11), which contributes to the landward shift in the salinity intrusion.

4. Discussion

Using a realistic configuration and a nested, high-resolution hydrodynamic model, we quantify potential impacts of storm surge barriers on a partially mixed estuary. Compared with existing surge barriers, the conceptualized barrier at Verrazano Narrows would be distinctive in terms of its size and the type of estuary. The primary navigational gated opening would be larger than any existing barrier, and the total area open to flow would be relatively large at almost 60%. Most of the existing barriers have cumulative gated openings that are much less than half the

total barrier length, the main exception being the Venice MOSE project that uses inflatable flap gates (Mooyaart & Jonkman, 2017).

The relatively large open cross-sectional area results in modest decreases in tidal amplitude compared to other barriers. The decrease in tidal amplitude in the estuary averages 2%–7%, which during spring tides corresponds to decreases in high water ranging from 8 cm in the lower estuary to 3 cm in the tidal river. Tidal marshes along the Hudson are located in the upper half of the tidal frame, with low marsh elevations centered around mean high water (Tabak et al., 2016). Marshes are inundated primarily during spring tides, so modest reductions in spring tide water levels can result in proportionally greater reduction in marsh inundation, potentially affecting sediment delivery and ecosystem function. For example, Piermont (37 rkm) is a salt marsh and Tivoli (156 rkm) and Schodack (212 rkm) are tidal fresh marshes that are part of the Hudson National Estuarine Research Reserve (Yellen et al., 2021). Potential effects on inundation frequency at these marshes are assessed by comparing the mean elevation of the marsh platforms with the tidal water levels in the simulations. The model does not include wetting-and-drying nor does it simulate inundation of the marshes, so the analysis is based on water levels adjacent to the marsh locations. For low and moderate discharge, the fraction of tides above the marsh elevation is reduced by about 25% for the Piermont and Tivoli marshes and by about 10% for the Schodack marsh. For the high discharge case the effect of the barrier on the inundation frequency is less with reductions of 5%–10% because the mean water surface along the estuary is higher due to the greater river flow.

The increased tidal velocities through the gated opening are potentially of concern for navigational and environmental impacts. Maximum surface velocities in the barrier case are over 2.5 m s^{-1} , exceeding the typical design aim for navigation of 1.5 m s^{-1} (Mooyaart & Jonkman, 2017). Similarly, a design study for a barrier in Boston Harbor calculated maximum tidal velocities up to 2.4 m s^{-1} and noted potential challenges to navigation for small vessels (Kirshen et al., 2018). Increased tidal velocities can cause increased bed scour, requiring protection measures and maintenance as for barriers in Germany and the Netherlands (Mooyaart & Jonkman, 2017), or potentially remobilizing contaminated bed sediments of the Upper Bay into the water column (Rodenburg & Ralston, 2017; Steinberg et al., 2004).

The increase in total drag with the barriers is not due primarily to increased bottom friction, but instead flow separation and eddy generation downstream of the barrier piers that causes form drag. Form drag is a major factor in other shallow flows with bathymetric complexity, including tidal flow around headlands (Edwards et al., 2004; McCabe et al., 2006; Warner & MacCready, 2014), over ridges or sills (Horwitz et al., 2021; MacKinnon et al., 2019; Nash & Moum, 2001), and through channel bends (Bo & Ralston, 2020). To characterize the role of form drag compared with bottom friction we follow an approach used to scale form drag from tidal flow past a headland (McCabe et al., 2006). The drag force depends on the pressure gradient created by the water surface anomalies in the eddies downstream of the barrier piers. Using the maximum tidal velocity through the barrier openings to scale the surface perturbations and the projected frontal area of the barrier piers, form drag scales as

$$D_{form} \sim \rho U_{\theta}^2 W_{bar} H_{bar} \quad (9)$$

where U_{θ} is the flow through the barrier openings, and W_{bar} and H_{bar} are the width and depth of the barrier piers. For bottom friction, the drag is represented with a drag coefficient C_f as in Equation 3,

$$D_{bot} \sim \rho C_f U_i^2 W_{bot} L_{bot} \quad (10)$$

where U_i is the average tidal velocity in the region, and W_{bot} and L_{bot} are the width and along-channel distance of the control volume. For the bottom friction drag, representative values are $C_f = 0.0025$, $W_{bot} = 3 \text{ km}$, $L_{bot} = 2 \text{ km}$, and $U_i = 1.0 \text{ m s}^{-1}$. The constrictions of the barrier openings cause local increase in velocity by a factor of 2 (Figure 3), so $U_{\theta} \approx 2U_i$. The average depth at the barriers is $H_{bar} = 15 \text{ m}$, and the cumulative pier width is $W_{bar} = 1,400 \text{ m}$. Based on these values, the ratio D_{form}/D_{bot} is 5.6, which is similar to the ratio of the total drag to that frictional drag of about 5 (Figure 6).

Alternatively, the form drag can be written in terms of a bluff body drag coefficient C_{bb} :

$$D_{form} = \frac{1}{2} \rho C_{bb} U_i^2 W_{bar} H_{bar} \quad (11)$$

Using the average tidal velocity and the cross-sectional area of the piers (MacCready & Pawlak, 2001). The bluff body drag coefficient required to have form drag that is a factor of 5 greater than the bottom friction is $C_{bb} = 7$. For comparison, the bluff body drag coefficient for tidal flow around a headland in Puget Sound was found to be about 9 (Warner & MacCready, 2009), and for flow over a sharp sill in the Bay of Fundy the bluff body drag coefficient was found to be 3–4 (Horwitz et al., 2021). The estimated drag coefficient for the barrier is similar to the drag coefficients for these other tidally energetic flows and sharp bathymetric features, which provides guidance for scaling the drag impacts of other barriers.

The enhanced mixing in the vicinity of the barrier also is analogous to that at sills or constrictions, where increased tidal velocities provide energy for mixing. In this case, the increase in mixing is large enough to affect the exchange flow by mixing seaward flowing, near-surface water downward into the landward-flowing lower layer. Similar reflux occurs due to intensified mixing at sills in Puget Sound, and the recirculation of upper layer can increase residence time in the estuary by 10%–30% (MacCready et al., 2021). The reduction in tidal amplitude also increases the stratification in the estuary, so the combination of increased residence time and increased stratification could affect biogeochemical processes in the estuary as well as distributions of nutrients and dissolved oxygen.

The landward shift in the salinity distribution and increase in stratification could affect the ecosystem function, as seen with changes in zooplankton and marsh vegetation linked to salinity changes with the Eastern Scheldt barrier (Bakker et al., 1990; de Leeuw et al., 1994). The simulated changes in salinity intrusion in the Hudson with the barriers are relatively modest and are much less than the landward shifts that have resulted from channel deepening for navigation. Since major dredging efforts began in the late 1800s, channel depths in the Harbor and lower Hudson have increased by 10%–30%, and this overall deepening has increased the estuarine circulation, increased stratification, and caused landward movement of the salinity intrusion by about 30% (Ralston & Geyer, 2019). The more modest projected impacts of the barrier on the salinity intrusion from these model results are comparable to those for the recent channel deepening completed in 2016 that increased controlling depths in the Harbor from 45 to 50 ft. For example, the barrier increased the salinity intrusion in the low discharge case ($125 \text{ m}^3 \text{ s}^{-1}$) by 4–6 km (Figure 7), and model results indicated that the recent harbor deepening increased the salinity intrusion by about 5 km at similarly low discharge ($150 \text{ m}^3 \text{ s}^{-1}$) (Hoagland et al., 2020; Ralston & Geyer, 2019). Such landward shifts in the salinity intrusion in the Hudson have the potential to increase the risk of contamination municipal drinking water supplies with intakes along the tidal Hudson. For example, the harbor deepening was found to increase the risk of salinity threatening the drinking water intake for the Poughkeepsie, NY (112 rkm), increasing potential mitigation costs (Hoagland et al., 2020). A similar approach could be used to assess how landward shifts in the salinity intrusion from surge barriers could alter conditions at drinking water intakes in the Hudson and other estuaries.

An additional consideration for the impacts on the New York Harbor and the Hudson is that the storm surge protection plan would also likely include barriers at Throgs Neck in the East River and in Arthur Kill to the west of Staten Island, in addition to Verrazano Narrows (US Army Corps of Engineers, 2019). The other barriers are smaller and likely have less influence on the tidal and estuarine dynamics, but increased drag and mixing would be expected there as well. The combination of the Verrazano Narrows, Throgs Neck, and Arthur Kill barriers represents just one of several alternatives being considered for storm damage risk reduction in the New York Harbor area. Other approaches include an Outer Harbor barrier between Sandy Hook and Breezy Point that would span nearly 9-km, as well as alternatives with multiple smaller barriers located inside the Harbor (US Army Corps of Engineers, 2019). The impacts on the tides and circulation in the estuary of each alternative are likely to depend on barrier locations and the reductions in flow cross-sectional area.

The modeling approach aimed to simulate realistic conditions by using a nested model and barrier configuration based on a conceptualized design, but the range of scales between the barrier (gated openings of 10s of m) and the estuary (length scales of 100s of km) remains challenging to resolve. The horizontal grid resolution in the inner grid was about 20 m, but even higher grid resolution would have better represented the flow through the smaller openings. Flow separation and form drag likely depends on the design of the barrier piers, which was simplified for the model resolution here. Constructed barriers could include design features to streamline the piers and reduce flow disturbance, potentially reducing the drag. Higher resolution modeling of pier designs would be needed to evaluate their influence on the larger scale dynamics, including nonhydrostatic effects. Vortices shed downstream of the piers have horizontal length scales similar to pier widths and can be greater than the water

depth, and thus have characteristics of 2-d turbulence in shallow flows (Uijttewaal & Jirka, 2003). In shallow flows the depth constrains the vertical dimension, and turbulent kinetic energy is transferred to larger scales rather than an energy cascade from larger to smaller scales and dissipation with 3-d turbulence. Reynolds-averaged models can simulate shallow flows downstream of piers, but they must be able to represent interactions between the 2-d eddies and the 3-d turbulence from the bottom boundary layer with a fully 3-d k-epsilon style turbulence closure (Kimura et al., 2009). Reynolds-averaged Navier-Stokes models with 3-d turbulence closure could better represent the lateral eddy viscosity of these large-scale vortices, but such models require much higher resolution than is possible at the estuary scale and typically include simplifications like a rigid lid or idealized domain. How the details of the barrier structure design influence the flow locally and then at larger scales remains an important gap in our understanding of their potential environmental impacts.

5. Summary

A realistic, high-resolution model of storm surge barriers for New York Harbor is used to quantify potential impacts on conditions in the Hudson River estuary. Flow constriction through gated openings causes local increases in maximum tidal velocities by more than a factor of 2. The barrier structures also increase the hydrodynamic drag, which results in decreased tidal amplitude landward of the barrier. For the conceptualized barrier configuration, the tidal amplitude decrease is about 6% in the lower estuary and about 2% farther landward, with corresponding decreases in tidal velocity and high-water levels. The total drag near the barriers increases by a factor of 5, primarily due to form drag from flow separation at the barrier piers rather than increased bottom friction. The effective bluff-body drag coefficient for the barrier is similar to that for natural topographic features like headlands and sills in other estuaries.

The increased tidal velocities through barrier openings results in increased salinity mixing near the barriers. In contrast, decreased tidal amplitude in the estuary results in decreased salinity mixing. As a result, the stratification, exchange flow, and length of the salinity intrusion all increase moderately inside the estuary. Increased mixing near the barriers causes reflux of surface water into the lower layer, locally increasing the exchange flow and potentially increasing residence times.

The changes in estuarine dynamics are not large enough to cause a major regime shift, in that it remains a partially mixed estuary with the barriers. Due to the linkages among the flow constriction, tidal velocity, drag, mixing, and the exchange flow, the estuarine response to a storm surge barrier depends centrally on the fraction of the cross-section with gated openings for tidal flow, a key consideration in transferring results to other partially mixed estuaries. Uncertainties remain regarding interactions between the tidal flow and barrier structures that require modeling approaches with higher resolution and added dynamical complexity to represent key physical processes at length scales on the order of the water depth.

Data Availability Statement

Data for the manuscript are posted at <https://doi.org/10.5281/zenodo.5703524>.

References

- Abood, K. A. (1974). Circulation in the Hudson Estuary. *Annals of the New York Academy of Sciences*, 250, 39–111. <https://doi.org/10.1111/j.1749-6632.1974.tb43895.x>
- Bakker, C., Herman, P. M. J., & Vink, M. (1990). Changes in seasonal succession of phytoplankton induced by the storm-surge barrier in the Oosterschelde (SW Netherlands). *Journal of Plankton Research*, 12, 947–972. <https://doi.org/10.1093/plankt/12.5.947>
- Bo, T., & Ralston, D. K. (2020). Flow separation and increased drag coefficient in estuarine channels with curvature. *Journal of Geophysical Research: Oceans*, 125(10). e2020JC016267. <https://doi.org/10.1029/2020jc016267>
- Bowen, M. M., & Geyer, W. R. (2003). Salt transport and the time-dependent salt balance of a partially stratified estuary. *Journal of Geophysical Research*, 108, 3158. <https://doi.org/10.1029/2001JC001231>
- Brand, A. D., Kothuis, B., & Prooijen, B. (2016). *The Eastern Scheldt Survey. A concise overview of the estuary pre- and post barrier Part 2. SURVEY*. <https://doi.org/10.13140/RG.2.1.1455.5764>
- Burchard, H., Bolding, K., Feistel, R., Gräwe, U., Klingbeil, K., Parker, M. C., et al. (2018). The Knudsen theorem and the Total Exchange Flow analysis framework applied to the Baltic Sea. *Progress in Oceanography*, 165, 268–286. <https://doi.org/10.1016/j.poccean.2018.04.004>
- Burchard, H., & Rennau, H. (2008). Comparative quantification of physically and numerically induced mixing in ocean models. *Ocean Modelling*, 20, 293–311. <https://doi.org/10.1016/j.ocemod.2007.10.003>
- Chen, S.-N., Geyer, W. R., Ralston, D. K., & Lerczak, J. A. (2012). Estuarine exchange flow quantified with isohaline coordinates: Contrasting long and short estuaries. *Journal of Physical Oceanography*, 42, 748–763. <https://doi.org/10.1175/jpo-d-11-086.1>

Acknowledgments

Funding from Hudson Research Foundation (Award #003/19A). Thanks to Brian Yellen for marsh elevation data and Philip Orton for helpful feedback on a draft of the manuscript.

- Chen, Z., Orton, P., & Wahl, T. (2020). Storm surge barrier protection in an era of accelerating sea-level rise: Quantifying closure frequency, duration and trapped river flooding. *Journal of Marine Science and Engineering*, 8, 725. <https://doi.org/10.3390/jmse8090725>
- Conroy, T., Sutherland, D. A., & Ralston, D. K. (2020). Estuarine exchange flow variability in a seasonal, segmented estuary. *Journal of Physical Oceanography*, 50, 595–613. <https://doi.org/10.1175/jpo-d-19-0108.1>
- de Leeuw, J., Leo, P. A., Herman, P. M. J., de Munck, W., & Beertink, W. G. (1994). The response of salt marsh vegetation to tidal reduction caused by the Oosterschelde storm-surge barrier. In P. H. Nienhuis & A. C. Smaal (Eds.), *The Oosterschelde estuary (The Netherlands): A case-study of a changing ecosystem. Developments in hydrobiology* (pp. 335–353). Springer Netherlands. https://doi.org/10.1007/978-94-011-1174-4_25
- de Vet, P. L. M., van Prooijen, B. C., & Wang, Z. B. (2017). The differences in morphological development between the intertidal flats of the Eastern and Western Scheldt. *Geomorphology*, 281, 31–42. <https://doi.org/10.1016/j.geomorph.2016.12.031>
- Du, J., Shen, J., Bilkovic, D. M., Hershner, C. H., & Sisson, M. (2017). A numerical modeling approach to predict the effect of a storm surge barrier on hydrodynamics and long-term transport processes in a partially mixed estuary. *Estuaries and Coasts*, 40, 387–403. <https://doi.org/10.1007/s12237-016-0175-0>
- Ebbesmeyer, C. C., & Barnes, C. A. (1980). Control of a fjord basin's dynamics by tidal mixing in embracing sill zones. *Estuarine and Coastal Marine Science*, 11, 311–330. [https://doi.org/10.1016/s0302-3524\(80\)80086-7](https://doi.org/10.1016/s0302-3524(80)80086-7)
- Edwards, K. A., MacCready, P., Moum, J. N., Pawlak, G., Klymak, J. M., & Alexander, P. (2004). Form drag and mixing due to tidal flow past a sharp point. *Journal of Physical Oceanography*, 34, 1297–1312. [https://doi.org/10.1175/1520-0485\(2004\)034<1297:fdamdt>2.0.co;2](https://doi.org/10.1175/1520-0485(2004)034<1297:fdamdt>2.0.co;2)
- Fischer, H. (1972). Mass transport mechanisms in partially stratified estuaries. *Journal of Fluid Mechanics*, 53, 671–687. <https://doi.org/10.1017/S0022112072000412>
- Geyer, W. R., & Nepf, H. M. (1996). Tidal pumping of salt in a moderately stratified estuary. In D. G. Aubrey & C. T. Friedrichs (Eds.), *Buoyancy effects on coastal and estuarine dynamics* (pp. 213–226). American Geophysical Union. <https://doi.org/10.1029/ce053p0213>
- Geyer, W. R., & Signell, R. P. (1992). A reassessment of the role of tidal dispersion in estuaries and Bays. *Estuaries*, 15, 97–108. <https://doi.org/10.2307/1352684>
- Haidvogel, D. B., Arango, H., Budgell, W. P., Cornuelle, B. D., Curchitser, E., Di Lorenzo, E., et al. (2008). Ocean forecasting in terrain-following coordinates: Formulation and skill assessment of the Regional Ocean modeling system. *Journal of Computational Physics*, 227, 3595–3624. <https://doi.org/10.1016/j.jcp.2007.06.016>
- Hoagland, P., Beet, A., Ralston, D. K., Parsons, G. R., Shirazi, Y. A., & Carr, E. W. (2020). Salinity intrusion in a modified river-estuary system: An integrated modeling framework for source-to-sea management. *Frontiers in Marine Science*, 7, 425. <https://doi.org/10.3389/fmars.2020.00425>
- Horvitz, R. M., Taylor, S., Lu, Y., Paquin, J.-P., Douglas, S., & Greenberg, D. A. (2021). Rapid reduction of tidal amplitude due to form drag in a narrow channel. *Continental Shelf Research*, 213, 104299. <https://doi.org/10.1016/j.csr.2020.104299>
- Kimura, I., Uijtewaal, W. S., Hosoda, T., & Ali, M. S. (2009). URANS computations of shallow grid turbulence. *Journal of Hydraulic Engineering*, 135, 118–131. [https://doi.org/10.1061/\(ASCE\)0733-9429\(2009\)135:2\(118\)](https://doi.org/10.1061/(ASCE)0733-9429(2009)135:2(118))
- Kirshen, P., Thurson, K., McMann, B., Foster, C., Sprague, H., Roberts, H., et al. (2018). *Feasibility of harbor-wide barrier systems: Preliminary analysis for Boston harbor*. University of Massachusetts.
- Kluijver, M., Dols, C., Jonkman, S. N., & Mooyaart, L. F. (2019). Advances in the planning and conceptual design of storm surge barriers—Application to the New York metropolitan area. *Coastal Structures*, 326–336. https://doi.org/10.18451/978-3-939230-64-9_033
- Lentz, S. J., Davis, K. A., Churchill, J. H., & DeCarlo, T. M. (2017). Coral reef drag coefficients—water depth dependence. *Journal of Physical Oceanography*, 47, 1061–1075. <https://doi.org/10.1175/jpo-d-16-0248.1>
- Lerczak, J. A., Geyer, W. R., & Chant, R. J. (2006). Mechanisms driving the time-dependent salt flux in a partially stratified estuary. *Journal of Physical Oceanography*, 36, 2296–2311. <https://doi.org/10.1175/jpo2959.1>
- Lerczak, J. A., Geyer, W. R., & Ralston, D. K. (2009). The temporal response of the length of a partially stratified estuary to changes in river flow and tidal amplitude. *Journal of Physical Oceanography*, 39, 915–933. <https://doi.org/10.1175/2008jpo3933.1>
- Lorenz, M., Klingbeil, K., MacCready, P., & Burchard, H. (2019). Numerical issues of the Total Exchange Flow (TEF) analysis framework for quantifying estuarine circulation. *Ocean Science*, 15, 601–614. <https://doi.org/10.5194/os-15-601-2019>
- MacCready, P. (2011). Calculating estuarine exchange flow using isohaline coordinates. *Journal of Physical Oceanography*, 41, 1116–1124. <https://doi.org/10.1175/2011jpo4517.1>
- MacCready, P., Geyer, W. R., & Burchard, H. (2018). Estuarine exchange flow is related to mixing through the salinity variance budget. *Journal of Physical Oceanography*, 48, 1375–1384. <https://doi.org/10.1175/jpo-d-17-0266.1>
- MacCready, P., McCabe, R. M., Siedlecki, S. A., Lorenz, M., Giddings, S. N., Bos, J., et al. (2021). Estuarine circulation, mixing, and residence times in the Salish Sea. *Journal of Geophysical Research: Oceans*, 126, e2020JC016738. <https://doi.org/10.1029/2020jc016738>
- MacCready, P., & Pawlak, G. (2001). Stratified flow along a corrugated slope: Separation drag and wave drag. *Journal of Physical Oceanography*, 31, 2824–2839. [https://doi.org/10.1175/1520-0485\(2001\)031<2824:SFAACS>2.0.CO;2](https://doi.org/10.1175/1520-0485(2001)031<2824:SFAACS>2.0.CO;2)
- MacKinnon, J. A., Alford, M. H., Voet, G., Zeiden, K. L., Johnston, T. M. S., Siegelman, M., et al. (2019). Eddy wake generation from broadband currents near Palau. *Journal of Geophysical Research: Oceans*, 124, 4891–4903. <https://doi.org/10.1029/2019JC014945>
- McCabe, R. M., MacCready, P., & Pawlak, G. (2006). Form drag due to flow separation at a headland. *Journal of Physical Oceanography*, 36, 2136–2152. <https://doi.org/10.1175/JPO2966.1>
- Mooyaart, L. F., & Jonkman, S. N. (2017). Overview and design considerations of storm surge. *Barriers Journal of Waterway, Port, Coastal, and Ocean Engineering*, 143, 06017001. [https://doi.org/10.1061/\(ASCE\)WW.1943-5460.0000383](https://doi.org/10.1061/(ASCE)WW.1943-5460.0000383)
- Mukai, A. Y., Westerink, J. J., Luettich, R. A., Jr., & Mark, D. (2002). *Eastcoast 2001, a tidal constituent database for western north atlantic, gulf of Mexico, and caribbean sea*. DTIC Document.
- Nash, J. D., & Moum, J. N. (2001). Internal hydraulic flows on the continental shelf: High drag states over a small bank. *Journal of Geophysical Research*, 106, 4593–4611. <https://doi.org/10.1029/1999JC000183>
- Nienhuis, P. H., & Smaal, A. C. (1994). The Oosterschelde estuary, a case-study of a changing ecosystem: An introduction. *The Oosterschelde estuary (The Netherlands): A case-study of a changing ecosystem* (pp. 1–14). Springer. https://doi.org/10.1007/978-94-011-1174-4_1
- Orton, P. M., Hall, T. M., Talke, S. A., Blumberg, A. F., Georgas, N., & Vinogradov, S. (2016). A validated tropical-extratropical flood hazard assessment for New York Harbor. *Journal of Geophysical Research: Oceans*, 121, 8904–8929. <https://doi.org/10.1002/2016JC011679>
- Ralston, D. K., Cowles, G. W., Geyer, W. R., & Holleman, R. C. (2017). Turbulent and numerical mixing in a salt wedge estuary: Dependence on grid resolution, bottom roughness, and turbulence closure. *Journal of Geophysical Research: Oceans*, 122, 692–712. <https://doi.org/10.1002/2016JC011738>
- Ralston, D. K., & Geyer, W. R. (2019). Response to channel deepening of the salinity intrusion, estuarine circulation, and stratification in an urbanized estuary. *Journal of Geophysical Research: Oceans*, 124, 4784–4802. <https://doi.org/10.1029/2019JC015006>

- Ralston, D. K., Geyer, W. R., & Lerczak, J. A. (2008). Subtidal salinity and velocity in the Hudson River estuary: Observations and modeling. *Journal of Physical Oceanography*, *38*, 753–770. <https://doi.org/10.1175/2007jpo3808.1>
- Ralston, D. K., Geyer, W. R., & Warner, J. C. (2012). Bathymetric controls on sediment transport in the Hudson River estuary: Lateral asymmetry and frontal trapping. *Journal of Geophysical Research*, *117*, C10013. <https://doi.org/10.1029/2012JC008124>
- Ralston, D. K., Warner, J. C., Geyer, W. R., & Wall, G. R. (2013). Sediment transport due to extreme events: The Hudson River estuary after tropical storms Irene and Lee. *Geophysical Research Letters*, *40*, 5451–5455. <https://doi.org/10.1002/2013GL057906>
- Rayson, M. D., Gross, E. S., Hetland, R. D., & Fringer, O. B. (2017). Using an isohaline flux analysis to predict the salt content in an unsteady estuary. *Journal of Physical Oceanography*, *47*, 2811–2828. <https://doi.org/10.1175/jpo-d-16-0134.1>
- Rennau, H., & Burchard, H. (2009). Quantitative analysis of numerically induced mixing in a coastal model application. *Ocean Dynamics*, *59*, 671–687. <https://doi.org/10.1007/s10236-009-0201-x>
- Rodenburg, L. A., & Ralston, D. K. (2017). Historical sources of polychlorinated biphenyls to the sediment of the New York/New Jersey Harbor. *Chemosphere*, *169*, 450–459. <https://doi.org/10.1016/j.chemosphere.2016.11.096>
- Shchepetkin, A. F., & McWilliams, J. C. (2005). The regional oceanic modeling system (ROMS): A split-explicit, free-surface, topography-following-coordinate oceanic model. *Ocean Modelling*, *9*, 347–404. <https://doi.org/10.1016/j.ocemod.2004.08.002>
- Steinberg, N., Suszkowski, D. J., Clark, L., & Way, J. (2004). *Health of the Harbor. The first comprehensive look at the State of the NY/NJ Harbor estuary*. A report to the NY/NJ Harbor Estuary Program. Hudson River Foundation.
- Strauss, B. H., Orton, P. M., Bittermann, K., Buchanan, M. K., Gilford, D. M., Kopp, R. E., et al. (2021). Economic damages from Hurricane Sandy attributable to sea level rise caused by anthropogenic climate change. *Nature Communications*, *12*, 2720. <https://doi.org/10.1038/s41467-021-22838-1>
- Sutherland, D. A., MacCready, P., Banas, N. S., & Smedstad, L. F. (2011). A model study of the Salish Sea estuarine circulation. *Journal of Physical Oceanography*, *41*, 1125–1143. <https://doi.org/10.1175/2011JPO4540.1>
- Tabak, N. M., Laba, M., & Spector, S. (2016). Simulating the effects of sea level rise on the resilience and migration of tidal wetlands along the Hudson River. *PLoS One*, *11*, e0152437. <https://doi.org/10.1371/journal.pone.0152437>
- Talke, S. A., Orton, P., & Jay, D. A. (2014). Increasing storm tides in New York harbor, 1844–2013. *Geophysical Research Letters*, *41*, 3149–3155. <https://doi.org/10.1002/2014gl059574>
- Temmerman, S., Meire, P., Bouma, T. J., Herman, P. M. J., Ysebaert, T., & De Vriend, H. J. (2013). Ecosystem-based coastal defence in the face of global change. *Nature*, *504*, 79–83. <https://doi.org/10.1038/nature12859>
- Uijtewaal, W. S. J., & Jirka, G. H. (2003). Grid turbulence in shallow flows. *Journal of Fluid Mechanics*, *489*, 325–344. <https://doi.org/10.1017/S0022112003005020>
- US Army Corps of Engineers. (2019). *New York—New Jersey harbor and tributaries coastal storm risk management feasibility study—Overview of engineering work for the NYNJHATS Interim report*.
- US Army Corps of Engineers, Galveston District, and Texas General Land Office. (2021). *Coastal Texas protection and ecosystem restoration feasibility study—Final environmental impact statement*.
- US Army Corps of Engineers, Norfolk District, and City of Norfolk. (2018). *Final integrated city of Norfolk coastal storm risk management feasibility study/environmental impact statement*.
- US Army Corps of Engineers, Philadelphia District. (2021). *New Jersey Back Bays coastal storm risk management draft integrated feasibility report and Tier1 environmental impact statement*.
- van Rijn, L. C., & Leo, C. (2011). Analytical and numerical analysis of tides and salinities in estuaries; part I: Tidal wave propagation in convergent estuaries. *Ocean Dynamics*, *61*, 1719–1741. <https://doi.org/10.1007/s10236-011-0453-0>
- Vitousek, S., Barnard, P. L., Fletcher, C. H., Frazer, N., Erikson, L., & Storlazzi, C. D. (2017). Doubling of coastal flooding frequency within decades due to sea-level rise. *Scientific Reports*, *7*, 1399. <https://doi.org/10.1038/s41598-017-01362-7>
- Vousdoukas, M. I., Mentaschi, L., Voukouvalas, E., Verlaan, M., Jevrejeva, S., Jackson, L. P., & Feyen, L. (2018). Global probabilistic projections of extreme sea levels show intensification of coastal flood hazard. *Nature Communications*, *9*, 2360. <https://doi.org/10.1038/s41467-018-04692-w>
- Wahl, T., Haigh, I. D., Nicholls, R. J., Arns, A., Dangendorf, S., Hinkel, J., & Slangen, A. B. A. (2017). Understanding extreme sea levels for broad-scale coastal impact and adaptation analysis. *Nature Communications*, *8*, 16075. <https://doi.org/10.1038/ncomms16075>
- Wall, G., Nystrom, E., & Litten, S. (2008). Suspended sediment transport in the freshwater reach of the Hudson River estuary in eastern New York. *Estuaries and Coasts*, *31*, 542–553. <https://doi.org/10.1007/s12237-008-9050-y>
- Warner, J. C., Geyer, W. R., & Lerczak, J. A. (2005). Numerical modeling of an estuary: A comprehensive skill assessment. *Journal of Geophysical Research*, *110*, C05001. <https://doi.org/10.1029/2004JC002691>
- Warner, J. C., Geyer, W. R., Ralston, D. K., & Kalra, T. (2020). Using tracer variance decay to quantify variability of salinity mixing in the Hudson River estuary. *Journal of Geophysical Research: Oceans*, *125*, e2020JC016096. <https://doi.org/10.1029/2020JC016096>
- Warner, S. J., & MacCready, P. (2009). Dissecting the pressure field in tidal flow past a headland: When is form drag “real”? *Journal of Physical Oceanography*, *39*, 2971–2984. <https://doi.org/10.1175/2009jpo4173.1>
- Warner, S. J., & MacCready, P. (2014). The dynamics of pressure and form drag on a sloping headland: Internal waves versus eddies. *Journal of Geophysical Research: Oceans*, *119*, 1554–1571. <https://doi.org/10.1002/2013jc009757>
- Yellen, B., Woodruff, J. D., Ladlow, C., Ralston, D. K., Fernald, S., & Lau, W. (2021). Rapid tidal marsh development in anthropogenic backwaters. *Earth Surface Processes and Landforms*, *46*(3), 554–572. <https://doi.org/10.1002/esp.5045>

References From the Supporting Information

- Brier, G. W. (1950). Verification of forecasts expressed in terms of probability. *Monthly Weather Review*, *78*, 1–3.
- Murphy, A. H., & Epstein, E. S. (1989). Skill scores and correlation coefficients in model verification. *Monthly weather review* *117* (pp. 572–582). American Meteorological Society. [https://doi.org/10.1175/1520-0493\(1989\)117<0572:SSACCI>2.0.CO;2](https://doi.org/10.1175/1520-0493(1989)117<0572:SSACCI>2.0.CO;2)
- Wilmott, C. (1981). On the validation of models. *Physical Geography*, *2*, 184–194.